Huntingtin S421 phosphorylation increases kinesin and dynein engagement on early endosomes and lysosomes

Emily N. P. Prowse[1], Abdullah R. Chaudhary[1], David Sharon[1], Adam G. Hendricks[1]*

1. Bioengineering Department, McGill University, Montreal, QC, Canada

*adam.hendricks@mcgill.ca

Summary Statement

Huntingtin phosphorylation at S421 increases the outward motility of early endosomes and lysosomes by enhancing the microtubule binding and force generation of kinesin and dynein.

ABSTRACT

Huntingtin (htt) acts as a scaffolding protein that recruits motor proteins to vesicular cargoes, enabling it to regulate kinesin- and dynein-dependent transport. To maintain the native stoichiometry of huntingtin with its interacting partners, we used CRISPR/Cas9 to induce a phosphomimetic mutation of the endogenous htt at S421 (S421Dhtt). Using single-particle tracking, optical tweezers, and immunofluorescence, we examined the effects of this mutation on the motility of early endosomes and lysosomes. In S421Dhtt cells, early endosomes and lysosomes exhibited more outward motility towards the cell periphery compared to wild-type (WT) cells. In contrast, overexpression of htt had variable effects on the processivity, run length, and directional bias of both early endosomes and lysosomes. Kinesins and dyneins exerted greater forces on early endosomes and lysosomes in cells expressing S421Dhtt. Additionally, endosomes had higher binding rates, increased resistance to detachment under load, and enhanced recruitment of kinesins and dyneins in S421Dhtt cells. These data indicate that phosphorylation of the endogenous huntingtin causes early endosomes and lysosomes to move towards the cell periphery by activating both kinesins and dyneins.

List of Symbols and Abbreviations

α	Processivity parameter alpha
BDNF	Brain derived neurotrophic factor
DIC	Dynein intermediate chain
Early	Early endosome
EGF-qdot	Epidermal growth factor coated quantum dot
HD	Huntington's Disease
Htt	Huntingtin
KHC	Kinesin heavy chain
ks	Kolmogorov-Smirnov statistical test
latA	Latrunculin A
NZ	Nocodazole
R_g	Radius of gyration
S421Ahtt	Phosphoresistive huntingtin with the mutation S421A
S421Dhtt	Phosphomimetic huntingtin with the mutation S421D
WT+S421Dhtt	WT cells overexpressing mCherry-S421Dhtt
WT	Wild-type
WT+WThtt	WT cells overexpressing mCherry-WThtt

INTRODUCTION

Huntingtin (htt) is an essential, multifunctional, and ubiquitous protein. It consists of several disordered regions and 34 α-helical HEAT repeats (Fig. 1A) (Guo et al., 2018). Htt is essential for embryonic development (Duyao et al., 1995; Nasir et al., 1995; Schmitt et al., 1995; Zeitlin et al., 1995), and is ubiquitously expressed in tissues including the brain, ovaries, and testis into adulthood (Li et al., 1993; Sharp et al., 1995). It has diverse roles within the cell, including regulation of gene expression (Dunah et al., 2002; Futter et al., 2009; Holbert et al., 2001; Li et al., 2002; Marcora et al., 2003; Zuccato et al., 2003), cell morphology (Lo Sardo et al., 2012; Thion et al., 2015), cell survival (Leavitt et al., 2006), and intracellular transport (Cason et al., 2021; Gauthier et al., 2004; Liot et al., 2013; Twelvetrees et al., 2010; Wong and Holzbaur, 2014). Htt enhances transport of brain derived neurotrophic factor (BDNF) vesicles (Gauthier et al., 2004; Zala et al., 2008), autophagosomes in the mid-axon (Cason et al., 2021; Wong and Holzbaur, 2014), TrkB signalling vesicles (Liot et al., 2013), and synaptic vesicles through $GABA_R$ signalling (Twelvetrees et al., 2010). The remarkable ubiquity and variety of htt's roles underscore the importance of understanding its function in health and disease.

Teams of kinesins and dyneins transport signalling and degradative cargoes. There are multiple kinesins that drive outward transport towards microtubule plus ends at the cell periphery. Different ratios of kinesin-1, kinesin-2, and kinesin-3 associate with distinct cargo populations, allowing different motility characteristics for each population of vesicles (Bentley et al., 2015). Each type of kinesin has a unique binding rate and velocity, which leads combinations of motors to create a motility barcode for cargoes. Unlike kinesins, there is only one form of cytoplasmic dynein that drives organelle transport. Dynein forms a complex with dynactin and activating adaptors such as BicD, Hook1, and others to direct inward transport towards microtubule minus ends at the cell center (Cason et al., 2021; McKenney et al., 2014; Schlager et al., 2014). Scaffolding and adaptor proteins work together to regulate the recruitment and activity of both kinesin and dynein motors on each cargo based on its identity.

Huntingtin recruits teams of kinesin, dynein, and myosin VI motors to cargoes, allowing it to control the cargo's direction of movement along microtubules and switching between actin and microtubules (Caviston et al., 2011). Htt interacts with molecular motors indirectly through adaptors; kinesin-1 and the dynein adaptor dynactin interact with htt through HAP1 (Engelender, 1997; Li et al., 1998; McGuire et al., 2006; Twelvetrees et al., 2010), and myosin VI interacts through optineurin (Sahlender et al., 2005). In addition, dynein interacts directly with htt through its intermediate chain, suggesting a prominent role for htt in regulating inward transport (Caviston et al., 2007). Htt's interaction with myosin VI suggests htt regulates transitions to the actin cytoskeleton for short range transport or tethering. Upon htt deletion or mutation, intracellular transport of many vesicular cargoes is severely inhibited (Caviston and Holzbaur, 2009; Hilditch-Maguire, 2000).

Polyglutamine expansion mutations in htt lead to Huntington's disease (HD), disrupting multiple cellular functions and leading to neurodegeneration in medium spiny neurons of the striatum (Gil and Rego, 2008). HD mutations cause htt to form novel interactions. Notably, through increased self-association mutant htt forms aggregates throughout the cytoplasm and nucleus (Davies et al., 1997). These interactions cause aberrant initiation of autophagy, mTOR signalling, mitochondrial fission, and palmitoylation (reviewed in Wanker et al., 2019). Additional defects occur in neuronal transcription, endoplasmic reticulum homeostasis, mitochondrial function, calcium signalling, synaptic activity, and intracellular transport (reviewed in Saudou and Humbert, 2016), demonstrating the importance of htt's native interaction network in maintaining homeostasis (Colin et al., 2008; Lemarié et al., 2021; Zala et al., 2008).

Huntingtin is regulated by multiple post-translational modifications, including palmitoylation, phosphorylation, sumoylation, ubiquitination, and acetylation. The functions and mechanisms of many of these modifications remain unknown. Its palmitoylation site at C214, regulated by HIP14 in the Golgi, facilitates interactions with vesicular membranes (Yanai et al., 2006). Palmitoylation is reduced in cells expressing the polyglutamine-expanded htt protein that leads to HD, while restoring palmitoylation

reduces aggregation and cytotoxicity in vitro (Lemarié et al., 2021). Sumoylation sites may contribute to nuclear import and transcriptional regulation (Steffan et al., 2004). Ubiquitination and acetylation regulate huntingtin-mediated autophagy (Wong and Holzbaur, 2014). Htt has 40 known phosphosites, many of which have unknown biological functions (reviewed by Saudou and Humbert, 2016). The phosphorylation state of serine 421 affects axonal transport direction and velocity of BDNF vesicles and autophagosomes (Colin et al., 2008; Wong and Holzbaur, 2014), while mitochondrial transport is unaffected by this phosphosite (Xu et al., 2020). Each of htt's post-translational modifications contribute to its role in transport of both signaling and degradative cargoes. Further, post-translational modifications are reduced in HD, disrupting the balance of htt's interactions with its binding partners (Colin et al., 2008; Lemarié et al., 2021; Zala et al., 2008).

Post-translational modifications of scaffolding proteins can influence transport direction. The phosphomimetic mutation (S421Dhtt) mimics a constitutively phosphorylated amino acid and biased BDNF transport towards the cell periphery, while phosphoresistive mutations (S421Ahtt) led to increased transport towards the cell center (Colin et al., 2008). The S421Dhtt mutation is neuroprotective in cells with the mutation that leads to HD (Zala et al., 2008), which motivates our attempt to understand the native role of this phosphosite in cells with normal (WT) htt. It has also been generalized for various scaffolding proteins including RILP, Miro/TRAK1/TRAK2, JIP1, JIP3/4 that post-translational modifications can modify transport direction (Fu and Holzbaur, 2014). These studies suggest that huntingtin phosphorylation directs transport towards the cell periphery.

To elucidate the effects of S421 phosphorylation at native expression levels and determine the mechanisms of regulation for both early endosomes and lysosomes, we applied CRISPR-based gene editing and single-molecule biophysics. Previous studies analyzed the motility of cargoes overexpressing S421Dhtt or S421Ahtt constructs and performed Western blotting to determine S421's role in transport regulation (Colin et al., 2008; Zala et al., 2008). Western blot and immunofluorescence in overexpressing COS7

cells suggests that S421 phosphorylation increases the recruitment of kinesin to cargoes (Colin et al., 2008; Zala et al., 2008). However, only a subset of the motors bound to a cargo might be active (Encalada et al., 2011). In addition, the critical stoichiometry of interactions between scaffolding proteins and motors is disrupted in overexpression systems. We generated an endogenous mutation to replicate htt's native interactions and expression levels and observed its effect on organelle transport. We measured the forces generated by the motors driving early endosome and lysosome transport with optical tweezers to determine whether phosphorylation of huntingtin modifies motor activity. Single particle tracking allowed us to obtain nanometer-resolution tracking of cargo motility. Combining single-molecule biophysical approaches with gene editing provided mechanistic insight into htt's regulation of intracellular transport by S421 phosphorylation.

To understand how S421 phosphorylation of htt regulates intracellular transport, we examined early endosome and lysosome transport in CRISPR-generated S421Dhtt HEK293T cells. Motility assays demonstrated an increase in outward (microtubule plus-ended) motility for both early endosomes and lysosomes in cells expressing S421Dhtt. Additionally, lysosome run length increased upon S421 phosphorylation. Examining the forces generated by microtubule motors on early endosomes and lysosomes, we observed both kinesin and dynein motors had higher binding rates and increased resistance to unbinding under load with S421Dhtt for both cargoes. Cells with S421Dhtt showed higher forces in both outward and inward directions on both early endosomes and lysosomes. A higher fraction of kinesins and dyneins associated to microtubules upon S421 phosphorylation. The phosphorylation-induced change in directional bias and force generation for lysosomes was more subtle than those for early endosomes. We hypothesize that the native motility characteristics of the cargoes dictate the effect of S421 phosphorylation on htt: inward-directed early endosomes become bidirectional while bidirectional lysosomes increase their displacement. Our data indicates phosphorylation of htt at S421 increases motor recruitment and activity of early endosomes and lysosomes. Additionally, overexpression of WT and S421D htt suggests overexpressed htt disrupts the transport complex of htt, motors, and adaptors required for transport, affecting cargo run length, processivity, and direction.

RESULTS

Endogenous S421D mutation does not affect cytoskeletal organization or huntingtin localization

Introducing a phosphomimetic S421D mutation in the endogenous huntingtin did not alter huntingtin expression levels and localization or the organization of the cytoskeleton and golgi. In generating the S421D HEK293T cell line, we aimed to preserve the native expression levels and stoichiometry of interactions between htt and its many interactors. We used a lentiviral CRISPR cassette to generate this S421D point mutant cell line (Fig. 1B) and identified a single positive clone with the desired mutation using next-generation sequencing (Fig. 1C). S421Dhtt did not result in appreciable changes to the actin nor microtubule morphology (Fig. 1D). To determine whether S421Dhtt caused major defects in dynein function, we probed the organization of the Golgi apparatus (Burkhardt et al., 1997; Caviston et al., 2007; Corthésy-Theulaz et al., 1992). We observed no changes in the percentage of cells with organized versus dispersed Golgi, indicating dynein function was not severely disrupted (Fig. 1E). Importantly, the S421D mutation did not affect huntingtin's localization nor expression level (Fig. 1F, G). Overexpression of mCherry-WThtt or mCherry-S421Dhtt leads to elevated expression of both constructs at similar levels (Fig. 1G). In iPSC-derived neurons expressing polyglutamine-expanded huntingtin (180Q), S421Dhtt led to increased mitochondrial surface area while the number of mitochondria remained similar (Xu et al., 2020). Immunofluorescence of the mitochondria in HEK293T cells showed a decrease in the mitochondrial number and area upon S421D mutation (Fig. 1H-J), suggesting that S421Dhtt mitochondrial regulation may be cell-type dependent. Together, immunofluorescence and huntingtin expression level characterization demonstrated that the S421D mutation did not substantially alter the cytoskeleton, Golgi apparatus, nor localization of huntingtin while mitochondrial morphology was affected.

Huntingtin phosphorylation directs early endosomes towards the cell periphery

156 Introducing the S421D phosphomimetic mutation in the endogenous huntingtin gene
157 induced an outward directional bias in early endosomes but did not alter run length nor
158 processivity. We hypothesized that the processivity, run length, and fraction of outwardly-
159 directed early endosomes would increase upon S421 phosphorylation based on previous
160 work with BDNF vesicles in neurons (Colin et al., 2008). We quantified the processivity of
161 organelle trajectories using the slope of the log-log plot of mean-squared displacement
162 (α). For cargoes transported by microtubule-based motor proteins, we expect that $\alpha > 1$ is
163 indicative of directed transport, while $\alpha = 1$ indicates diffusive motion. The radius of
164 gyration (R_g) is an indicator of run length that determines the average position of a
165 trajectory and measures a radius containing half of the points in the trajectory from its
166 average position. We transfected cells with Rab5-eGFP to label early endosomes for
167 particle tracking (Fig. 2A, C). The endogenous S421D mutation increased the outward
168 motility of early endosomes towards the cell periphery without changing their processivity
169 or run length (Fig. 2E, F, I). The outward directional bias was previously described when
170 truncated WThtt and S421Dhtt were overexpressed in primary neurons (Colin et al., 2008;
171 Zala et al., 2008). To dissect the effects of htt phosphorylation and expression levels, we
172 transiently transfected full length mCherry-WThtt (WT+WThtt) or mCherry-S421Dhtt
173 (WT+S421Dhtt). These transfections lead to a ~4-10-fold increase in htt expression (Fig.
174 1G). Overexpression of S421Dhtt increased the processivity, run length, and
175 unexpectedly induced inward motility of early endosomes (Fig. 2E, F, I). Interestingly,
176 overexpression of WThtt increased the outward motility of early endosomes (Fig. 2I).
177 These unexpected results in overexpression conditions may be due to the change in
178 stoichiometry of htt's interactions with its native binding partners. The gene edited S421D
179 HEK293T cells demonstrate an outward bias of early endosomes, while htt
180 overexpression alters motility. This indicates that S421 phosphorylation is either recruiting
181 additional kinesins on early endosomes or increasing the activity of the kinesins present
182 on the early endosome.
183
184 **S421D increases run length and outward bias of lysosomes**
185

186 S421 phosphorylation increased lysosome run lengths and directed them toward the cell
187 periphery. We hypothesized S421Dhtt's effects to be universal for all htt-associated
188 cargoes, and therefore expected increased outward bias, processivity, and run length in
189 lysosomes. This hypothesis is supported by previous work showing that htt promotes
190 outward motility in the mid-axon of neurons for autophagosomes, which eventually mature
191 into lysosomes (Cason et al., 2021; Wong and Holzbaur, 2014). In both WT and S421D
192 experiments, the raw trajectories demonstrated the expected bidirectional motility (Fig.
193 2B, D). S421Dhtt induced an increase in run length and outward motility of lysosomes,
194 without affecting their processivity (Fig. 2G, H, J). When we overexpressed htt, we
195 observed a minor increase in processivity for WThtt and a substantial increase in run
196 length regardless of the phosphorylation state (Fig. 2G, H, J). Unexpectedly, WThtt
197 overexpression led to an inward directional bias (Fig. 2J), while overexpression of
198 S421Dhtt reversed the effect by increasing outward motility. Taken together, our results
199 indicate that htt overexpression modifies processivity, run length, and directional bias
200 while phosphorylation shifts lysosome motility towards the cell periphery and increases
201 their run length. This suggests S421 phosphorylation at native expression levels is
202 increasing the number of active kinesin motors, as was observed for early endosomes.
203
204 **Tethering on actin contributes to the directional bias of early endosomes**
205
206 Our results suggest that huntingtin's phosphorylation state modulates transient actin
207 tethering and contributes to the transport direction of early endosomes. Huntingtin
208 interacts with optineurin, which recruits myosin VI and could regulate cargo association
209 to actin (Sahlender et al., 2005). We used latrunculin A (latA) to depolymerize actin
210 filaments and reduce cargo association with actin. We expected an increase in run length
211 and processivity upon latA treatment since cargo tethering and confinement by actin are
212 reduced, allowing long range, processive motility by microtubule motors to dominate. We
213 determined the optimal concentration for motility assays via imaging cells labelled with
214 SiR-actin. We determined 250 nM latA was optimal as it resulted in significant
215 depolymerization of actin filaments without loss of native cellular morphology (Fig. S1A).
216 As expected, treatment with latA increased run length and processivity of Rab5 early

217 endosomes (Fig. S1B, C). Additionally, the phosphorylation-induced directional bias
218 became less prominent with latA, suggesting that short-range actin-based motility
219 contributes to the observed directional bias of early endosomes (Fig. S1D). WT early
220 endosomes have increased outward motility upon latA treatment, indicating that allowing
221 kinesin and dynein to dominate transport biases it outwards (Fig. S1D). The S421D
222 mutation did not further shift the directional bias in actin-depleted cells, suggesting that
223 both loss of actin tethering and htt phosphorylation act through similar mechanisms.
224
225 **Lysosomes have a higher dependence on microtubule-based transport**
226
227 Depolymerization of microtubules demonstrated no significant changes in processivity or
228 run length for early endosomes, while lysosomes showed significant decreases in both
229 run length and processivity. We used 10 μM nocodazole (NZ) to depolymerize
230 microtubules and observe how strongly the motility parameters were affected. We
231 expected that upon NZ treatment, both processivity and run length would decrease
232 because microtubule-based motors drive the long range processive transport of both
233 early endosomes and lysosomes. We observed this expected decrease in run length and
234 processivity for lysosomes, suggesting that they rely heavily on microtubule-based
235 transport to drive their motility (Fig. S1F, I, J). The large change in processivity and run
236 length for lysosomes demonstrates the magnitude of changes in these parameters upon
237 large scale disruption of the cytoskeleton. Early endosomes demonstrated a surprising
238 lack of effect of nocodazole treatment on their processivity and run length, perhaps due
239 to their inherently low processivity and run lengths compared to lysosomes (Fig. S1E, G,
240 H). The lysosomes in NZ-treated cells reached similar values for processivity and run
241 length to the early endosomes in the control condition, suggesting that the values for early
242 endosome motility were close to their minimum. Combining this result with our
243 conclusions from the latA treatment demonstrates that early endosome transport may be
244 more dependent on switching between actin-based and microtubule-based transport (Fig.
245 S1). These results indicate early endosome transport has a lower dependence on
246 microtubules compared to lysosomes, perhaps due to its inherently short run lengths and
247 lower processivity.

248

249 **S421 huntingtin phosphorylation activates kinesins and dyneins on early**
250 **endosomes**

251

252 To determine how changes in motor activity contribute to the motility we observed, we
253 measured the force generation of motors on early endosomes with optical tweezers. We
254 incubated cells with fibronectin-coated 500 nm polystyrene beads for 10-50 mins (Blocker
255 et al., 1997) and used optical tweezers to measure the forces that motors exerted in living
256 cells (Fig. 3A, B). At this stage of maturation, the early phagosomes (termed early
257 endosomes) are positive for Rab5 and other early endosome markers and represent a
258 subpopulation of the vesicles labeled by Rab5-eGFP. Early endosome force traces
259 demonstrated the expected bidirectional motility biased inwards (Fig. 3B). We predicted
260 kinesins would specifically be activated, or dyneins inactivated to generate the directional
261 bias we observed for early endosomes (Fig. 2I). Unexpectedly, the stall force distributions
262 for early endosomes shifted towards higher forces in both outward and inward directions
263 with S421Dhtt (Fig. 3C), suggesting both kinesins and dyneins were activated. In cells,
264 each kinesin motor exerts forces of 2-7 pN, and each dynein exerts approximately 2-3 pN
265 (Blehm et al., 2013). Looking closely at the distributions, we observe frequent kinesin
266 forces around 3 pN and 6 pN for cells with WThtt (Fig. 3C). Both of those populations are
267 observed in S421Dhtt cells, in addition to high force events near 9 pN and 12 pN.
268 Observing the inward directed forces, WT cells show frequent dynein forces near 1.5 pN
269 and 5 pN, while forces shift to ~ 3.5 pN, 9 pN, and 13 pN in S421Dhtt cells. Together,
270 these forces likely correspond to ~1-2 active kinesins and 1-3 active dyneins in WT cells,
271 and 1-4 active kinesins and 2-6 active dyneins in S421D cells, which is slightly lower than
272 previous estimates for late phagosomes (Chaudhary et al., 2018; Hendricks et al., 2010).
273 We then sought to determine how the force-dependent unbinding rates of each motor
274 were affected by S421Dhtt, predicting that the kinesin motors would have slower
275 unbinding and therefore induce the kinesin-based directional bias (Fig. 2I). The unbinding
276 rates of kinesin and dynein teams on early phagosomes in WT cells is similar (Fig. 3D,
277 Table S1). We observed slower unbinding under load of both kinesin and dynein teams
278 with S421Dhtt, consistent with more kinesin and dynein motors engaged with the

microtubule (Fig. 3D, Table S1). Next, we measured the binding rate of early endosomes moving inwards and outwards and found the binding rate for early endosomes was increased for both directions in S421Dhtt cells (Fig. 3G, H). The binding rate was more strongly enhanced for outward forces, suggesting an increased number of active kinesins enhances binding compared to WThtt (Fig. 3G). Observing the cumulative distribution functions, we note that outward and inward motor binding rates in S421Dhtt cells were very similar (Fig. 3H). This suggests that the kinesins are being activated to the same level as the dyneins, reducing the native inward bias for these cargoes. In summary, the force data indicate that huntingtin phosphorylation at site S421 increases the net force generation, affinity, and binding strength of both kinesin and dynein motors in early endosomes.

S421Dhtt increases lysosome microtubule binding and resistance to unbinding under load

Like for early endosomes, we hypothesized that kinesins would have increased activity on lysosomes as they also demonstrated an increased run length and outward directional bias (Fig. 2H, J). We measured the force characteristics of phagolysosomes by modifying the optical tweezers assay described for early endosomes with a longer incubation time of 1-2 hrs. The phagolysosomes measured in the optical tweezer experiments, termed lysosomes hereafter, represent a subpopulation of lysotracker-positive lysosomes, compared to our earlier analysis tracking all lysotracker-positive vesicles (Fig. 2). Sample force traces demonstrated typical bidirectional motility of lysosomes (Fig. 3B). We observed an increase in forces in both directions for lysosomes as for the early endosomes, although to a lesser degree (Fig. 3E). The balance of kinesin to dynein forces remained similar in both control and S421Dhtt conditions, as expected for these bidirectional cargoes. Predicting the number of motors as described for early endosomes, the force distributions suggest that 1-2 additional kinesins and 1-2 additional dyneins are engaged in S421Dhtt cells. The unbinding rates indicate that kinesin teams are more resistant to unbinding than dyneins for lysosomes (Fig. 3F). In S421Dhtt cells, we observed a slightly lower resistance to unbinding for lysosomes moving outward, while

310 the unbinding resistance was higher than WT for inward-moving cargoes (Fig. 3F, Table
311 S1). Finally, we examined the binding rates for lysosome motors to determine how
312 S421Dhtt affected microtubule affinity. S421Dhtt increased the binding rate for both
313 inward- and outward- directed cargoes compared to WT (Fig. 3I, J). The increased forces
314 and enhanced binding we observed in S421Dhtt cells suggests htt phosphorylation
315 recruits and/or activates both kinesins and dyneins.
316
317 **S421Dhtt increases kinesin and dynein association to microtubules**
318
319 As we did not observe increased kinesin activity compared to dynein upon S421
320 phosphorylation, we asked if more kinesins were engaged with microtubules to generate
321 the observed directional bias. We used immunofluorescence imaging to approximate the
322 differences in the number of motors associated with microtubules in each cell type. We
323 fixed the cells with methanol to remove cytosolic components and determine the relative
324 number of motors that were bound to microtubules in each condition at the time of fixation
325 (Fig. 4A, B). We then created intensity heatmaps of all images from the microtubules and
326 kinesin-1 heavy chain (KHC) or dynein intermediate chain (DIC) and plotted them on the
327 same axes (Fig. 4C-F). We detected higher intensities in the motors channel for both KHC
328 and DIC in the S421Dhtt cells (Fig. 4C-F). The higher intensity indicates a higher
329 concentration of motors on extracted microtubules in the S421Dhtt cells. Upon calculating
330 the correlation coefficients between the microtubule and motor channels for each
331 individual image, we observed that the dynein and microtubule intensities were more
332 highly correlated in S421Dhtt cells than WT cells. This assay demonstrates that S421Dhtt
333 increases the fraction of kinesin and dynein motors associated to microtubules. This
334 supports our data from the optical tweezers analysis, which showed a higher binding rate
335 and lower unbinding rate for motors in the S421Dhtt cells in both early endosomes and
336 lysosomes. Further, the signal for microtubule-bound kinesin and dynein motors is higher
337 in S421Dhtt cells, suggesting htt S421 phosphorylation increases the engagement of both
338 kinesins and dyneins with microtubules.
339
340 **DISCUSSION**

341

342 Our results show that huntingtin phosphorylation at S421 increases the number of active
343 kinesin and dynein motors on endosomes. Surprisingly, huntingtin activates microtubule
344 motors on endosomes at varying stages of maturation, from early endosomes to
345 lysosomes. Huntingtin also regulates the motility of neuronal signalling vesicles including
346 BDNF (Colin et al., 2008; Zala et al., 2008). In contrast, most cargo adaptors are recruited
347 to specific cargoes at specific stages of maturation (Cason et al., 2021; Mogre et al.,
348 2021). The ubiquitous function of huntingtin on a wide array of cargoes illustrates its role
349 as a central regulator of vesicular transport.

350

351 While kinesin and dynein teams exert more force and have enhanced microtubule binding
352 on both early endosomes and lysosomes in S421D huntingtin cells (Fig. 3,4), its effect on
353 the motility of different endocytic cargoes varies. For early endosomes, huntingtin
354 phosphorylation results in a pronounced shift in motility from primarily inward towards the
355 cell center to bidirectional motility (Fig. 2I). The processivity and displacement of early
356 endosomes are only weakly affected (Fig. 2E, F). In comparison, lysosomes display a
357 small but significant shift in motility towards the cell periphery in phosphomimetic htt cells
358 compared to control cells (Fig. 2J) while their run length is strongly enhanced (Fig. 2H).
359 Taken together, these results suggest that huntingtin phosphorylation regulates transport
360 by enhancing the activity of both kinesin and dynein (Fig. 5A, B). However, its effects on
361 the motility of different cargoes depend on their basal motility characteristics. In the basal
362 condition, early endosome motility is strongly biased towards the cell center. Activating
363 both kinesin and dynein results in a loss of the inward bias. Lysosome motility is
364 approximately equally distributed towards the cell center and periphery, such that
365 activating kinesin and dynein does not alter directionality, but rather increases the total
366 run length.

367

368 Disrupting actin filaments resulted in an increased outward motility similar to the effect of
369 S421Dhtt (Fig. S1A-D), suggesting a potential role for myosin VI-mediated tethering to
370 actin filaments (Sahlender et al., 2005) in generating the directional bias (Al-Haddad et
371 al., 2001). Yet, optical trapping and immunofluorescence show that S421Dhtt results in

372 enhanced forces and recruitment to microtubules for both kinesin and dynein (Figs. 3, 4),
373 suggesting S421D phosphorylation instead acts through activating microtubule motors.
374 Thus, we hypothesize that outward directional bias occurs in situations where microtubule
375 motors dominate transport. That could be achieved either by reducing tethering on actin
376 or by engaging more kinesins and dyneins.
377
378 Our findings are in broad agreement with previous studies showing that overexpressing
379 S421Dhtt resulted in increased outward motility of BDNF and TI-VAMP vesicles
380 compared to cells expressing phosphoresistive S421A htt constructs (Colin et al., 2008;
381 Zala et al., 2008). Further, Colin et al. observed increased kinesin-1 recruitment to
382 microtubules and enhanced interactions between the p150glued subunit of dynactin and
383 KHC upon S421Dhtt expression (Colin et al., 2008). Interestingly, we did not see KHC-
384 specific recruitment to microtubules with endogenous S421Dhtt compared to wild-type.
385 Instead, we observed an increase in recruitment of both motors, with slightly higher
386 dynein recruitment. These differences between previous results and our observations
387 may reflect effects of htt overexpression. Alternatively, they may be due to differences in
388 htt function in the embryonic kidney cells used here compared to previous studies in
389 neurons, which are highly polarized and have higher endogenous htt expression.
390
391 Overexpression of htt alters the processivity, run length, and directional bias of early
392 endosomes and lysosomes. The effects of overexpression are highly variable and often
393 do not reflect the trends observed when inducing mutations in the endogenous htt (Fig.
394 2), suggesting that maintaining the stoichiometry of htt to its many interacting proteins is
395 critical. We expect that excess htt in the cytoplasm is interacting with and sequestering
396 the motors and adaptors required to generate the effect that we observe in transport upon
397 overexpression (Fig. 5C). This result supports the known consequences of
398 overexpression experiments, which cause adverse effects by changing the stoichiometry
399 of interactions with other proteins in the cell. For example, overexpressing the p50
400 dynamitin subunit of dynactin causes a dominant negative effect in which early
401 endosomes and lysosomes become peripherally localized due to dynein sequestration
402 (Burkhardt et al., 1997). Regardless of the phosphorylation state, overexpression of htt

403 affected the directional bias of early endosomes and lysosomes. Processivity and run
404 lengths were increased for lysosomes in cells overexpressing either WT or S421Dhtt,
405 however, early endosomes only demonstrated this effect overexpressing S421Dhtt. This
406 work, supported by many previous studies discussing expression levels (e.g. (Burkhardt
407 et al., 1997; Dambournet et al., 2018)) highlights the importance of examining protein
408 function at endogenous expression levels to ensure biological relevance of the effects.
409 This is particularly important for scaffolding proteins like huntingtin, which mediates
410 interactions among many adaptors, effectors, motors, and membranes.
411
412 Transport is tightly regulated on multiple levels within the cell to ensure specific cargoes
413 arrive at their intracellular destination. Scaffolding proteins such as htt are a primary
414 mechanism of regulation that mediate interactions between cargoes and motor proteins,
415 and are the only known level of regulation that is cargo specific (Cason et al., 2021; Colin
416 et al., 2008; Fu and Holzbaur, 2014). Many scaffolds specifically interact with a limited
417 set of cargoes and are regulated by post-translational modifications (Cason et al., 2021;
418 Fu and Holzbaur, 2013; Fu and Holzbaur, 2014; Reed et al., 2006; Sun et al., 2017).
419 Here, we illustrate the role of htt in regulating early endosome and lysosome transport.
420 Htt S421 phosphorylation activates kinesin and dynein on both early endosomes and
421 lysosomes. However, enhanced kinesin and dynein activity differentially affects early
422 endosomes and lysosomes, influencing their direction, motor activity, and affinity for
423 microtubules. Our results underscore the central role of huntingtin in directing endosome
424 transport and suggest that huntingtin mutations likely result in cargo-specific disruptions
425 to both signalling and degradative pathways.
426
427 **MATERIALS AND METHODS**
428
429 **Cell Culture**
430 We passaged HEK293T cells (donated by Dr. Kamen's lab) at 80% or higher confluency
431 in a biosafety cabinet starting by rinsing with 2.5 mL 37 °C 1X phosphate buffered saline
432 (PBS, Wisent, St-Jean-Baptiste, QC, Canada), followed by adding 400 µL of 4 °C 0.25%
433 trypsin (Wisent) and incubating for 5 mins at 37 °C. Next, we used 5 mL of 37 °C complete
434 medium (Dulbecco's Modified Eagle Medium (DMEM), 10% fetal bovine serum (FBS), 2

435 mM Glutamax, 60 µg/mL penicillin 100 µg/mL streptomycin, all components from Gibco,
436 Waltham, MA, United States) to neutralize the trypsin activity. Finally, we placed a 1/5-
437 1/20 dilution of the resuspended cells in 37 °C fresh complete medium and transferred to
438 the 37 °C, 5% CO_2 incubator. We tested all stocks of cells for mycoplasma.
439
440 **CRISPR Design and Molecular cloning**
441 We transfected HEK293T cells with 1.25 µg of lentiCRISPR v2 cassette and 1.25 µg of
442 the single-stranded oligodeoxynucleotice (ssODN) for 24-36 hrs. lentiCRISPR v2 was a
443 gift from Feng Zhang (Addgene plasmid # 52961 ; http://n2t.net/addgene:52961 ;
444 RRID:Addgene_52961, Watertown, MA, United States) (Sanjana et al., 2014).
445 Subsequently, we selected expressing cells using 2 µg puromycin for 48-72 hrs. Finally,
446 we isolated single cells using fluorescence activated single cell sorting and grew them for
447 2-3 weeks in complete media containing 50% FBS. We verified clones containing the
448 S421D sequence with next-generation sequencing.
449
450 gRNA sequence:
451 GTTCCACAATACTCCCACTACGG
452 ssODN sequence:
453 ACGCCTCCACCCGAGCTTCTGCAAACCCTGACCGCAGTCGGGGGCATTGGGCAG
454 CTCACCGCTGCTAAGGAGGAGTCTGGTGGCCGATCTCGTAGTGGGGATATTGTGG
455 AACTTATAGGCAAGTTATTAGCAAGGTCTACTCTTACAATTAACTTTGCAGTAATAC
456 TAGTTACACTCTATTGATTATGGGCCTGCCCTGT
457 Sequencing primers:
458 Forward: CACCGTTCCACAATACTCCCACTA
459 Reverse: AAACTAGTGGGAGTATTGTGGAAC
460
461 **Plasmids and Transfection**
462 We transfected cells with 0.8 µg of eGFP-Rab5 or mCherry-S421D-htt or mCherry-WT-
463 htt huntingtin constructs 24-48 hrs before imaging. mCherry-S421D-htt and mCherry-WT-
464 htt constructs were generously donated from the Saudou lab, generated from the full
465 length pARIS-htt (Pardo et al., 2010) using methods from their previous work (Humbert

466 et al., 2002). We replaced cell culture medium in the 35 mm round glass bottom dishes
467 (Mattek, Ashland, MA, United States) containing the cells with 0.2 mL serum-free DMEM.
468 In separate 1.5 mL tubes, we added 2 µL/dish Lipofectamine 2000 (ThermoFisher
469 Scientific, Waltham, MA, United States) to 50 µL/dish serum-free DMEM and added 0.8
470 µg/dish of DNA to 50 µL/dish of serum-free DMEM. We then mixed the DNA and
471 lipofectamine, incubated for 20 mins at room temperature, and added 100 µL/dish to the
472 cells. Four hours later, we replaced the serum-free medium with complete media.
473
474 **Western Blotting**
475 We lysed cells by manually twisting while lifting and descending a Dounce homogenizer
476 20-30 times in 400 µL PBS containing 0.01 M dithiothreitol (DTT, R0681, ThermoFisher
477 Scientific) and 1X protease inhibitor cocktail (100X stock from PIC002, Bioshop,
478 Burlington, ON, Canada) on ice. Subsequently, we centrifuged the cell solution at 1500 g
479 for 10 mins at 4 °C, then centrifuged the supernatant at 16000 g for 10 mins at 4 °C. We
480 added 20 µL of lysate for each sample to the SDS-PAGE gel, diluted in 2x Laemmli buffer
481 (161-0737, Biorad, Hercules, CA, USA) with 2.5% 2-mercaptoethanol (M6250, Sigma,
482 Burlington, MA, United States) after heating to 100 °C for at least 10 mins. To mark
483 molecular weights, we loaded 5 µL of protein ladder (PI26634, ThermoFisher Scientific).
484 We used a 25 mM Tris (TRS001.1, Bioshop), 190 mM glycine (800-045-LG, Wisent), and
485 0.1% SDS (SDS999.100, Bioshop) running buffer, and ran the gel at 80 mA for 60-90
486 mins. To transfer, we used 25 mM Tris, 190 mM glycine, and 30% methanol (34860-4L-
487 R, Sigma) transfer buffer for wet transfer at 100 V for 90 mins with a PVDF membrane.
488 We blocked the membrane for 1 hour with blocking buffer: 5% bovine serum albumin
489 (BSA, Bioshop) in tris-buffered saline with Tween 20 (TBST, 20 mM Tris, 150 mM NaCl
490 (SOD004.1, Bioshop), 0.1% Tween 20 (P2287, Sigma). We diluted primary antibodies in
491 the blocking buffer and incubated at 4 °C overnight. Next, we washed the membrane with
492 blocking buffer 3 times for 5 mins and incubated with the secondary antibody diluted in
493 blocking buffer for 90 mins with constant agitation. We washed the membrane 3 times
494 with TBST before incubating with a 1:1 ratio of horseradish peroxidase substrate and
495 enzyme mixture (P90720, EMD Millipore, Burlington, MA, USA). We imaged using a
496 Biorad Chemidoc camera set to detect chemiluminescence. We subsequently stained the

497 membrane with Coomassie G-250 (CBB555.25, Bioshop), using a previously established
498 protocol from Goldman et al. titled Coomassie blue R-250 staining (Goldman et al., 2016).
499 We used the following primary antibodies: 1/1000 dilution of T9026 ms α-tubulin, Sigma
500 lot: 000089497, and 1/500 dilution of MAB2166 ms-huntingtin, Abcam, Cambridge,
501 England lot: 3703568. The secondary antibody was rabbit anti-mouse ab6728, Abcam.
502
503 **Motility Assay**
504 In a biological safety cabinet, we mixed 200 µL of 37 °C complete medium with
505 LysoTracker™ Deep Red (L12492, ThermoFisher Scientific) to a concentration of 70 nM
506 and added it to HEK293T cells in MatTek 35 mm glass bottom dishes. Cells were
507 incubated for 10 mins at 37 °C, and subsequently replaced the medium with 1 mL of 37
508 °C Lebovitz (11415064, Gibco) with 10 % FBS for imaging. We imaged cells in a 37°C
509 chamber of a Nikon Eclipse Ti-E microscope in near-total internal reflection (TIRF)
510 fluorescence settings using an EMCCD camera with an exposure time of 120 ms for 3
511 mins. We repeated the process for several cells within each dish and all cells were imaged
512 within 1 hour of adding the Lysotracker. For Rab5 transfected cells, we replaced the
513 medium with 0.5-1 mL of of 37 °C Lebovitz with 10 % FBS and imaged them as the
514 lysosomes. For experiments using 250 nM latrunculin A (S428021, Sigma) or 10 µM
515 nocodazole (M1404, Sigma), we added the drug to the Lebovitz medium a minimum of
516 15 mins prior to imaging.
517
518 **Immunofluorescence: Cytoskeleton and Golgi Apparatus**
519 This protocol was adapted from Jimenez et al. (Jimenez et al., 2020). We passaged
520 HEK293T cells onto rectangular coverslips (12544-A ThermoFisher Scientific) in 100 mm
521 petri dishes (83.3902, Sarstedt, Saint-Leonard, QC, Canada) ~24 hrs prior to fixation. We
522 performed incubations for extraction, fixing and $NaBH_4$ (452882, Sigma) solutions on flat
523 pieces of parafilm, with droplets containing 100 µL of the described solution. Using fine-
524 tipped tweezers, we manipulated the coverslips and placed them cell-side down on the
525 droplets. Firstly, we incubated the cell-adhered coverslips with 37 °C extraction solution
526 (0.25% Triton-X-100 (X100, Sigma), 0.1% glutaraldehyde (G5882, Sigma)) in PEM
527 (80mM PIPES (P6757, Sigma), 5mM EGTA (EGT101, Bioshop), 2mM $MgCl_2$ (M2866,

528 Sigma) at pH=6.8) for 15-45 s. We next fixed the cells with 37 °C 0.25% Triton-X-100 and
529 0.5% glutaraldehyde in PEM and incubated for 10 mins. We subsequently transferred the
530 coverslips to 0.1% $NaBH_4$ in PBS (Wisent) and incubated for 7 mins, then rinsed quickly
531 with PBS twice before blocking. Next, we incubated the fixed cells with blocking buffer
532 (2% BSA (ALB001, Bioshop) in PBS, (Wisent)) inside a glass petri dish for 30 mins with
533 gentle rocking on an orbital shaker. Subsequently, we added a 1:400 solution of primary
534 antibody in blocking buffer (anti-GM130 ab52649 Abcam, anti-tubulin Sigma T6199) in
535 100 µL droplets on a parafilm-coated humid chamber. We incubated coverslips with the
536 primary antibody droplets overnight at 4 °C. We then performed 3x 10-minute washes
537 with ~10 mL blocking buffer in glass petri dishes. After washing, we added a 1:400 dilution
538 of fluorescent secondary antibody, goat anti-mouse 594 (A11032, ThermoFisher) and
539 goat anti-rabbit (18772, Sigma), to the humid chamber with new parafilm and incubated
540 it for 1 hr at room temperature protected from light. We then washed as described after
541 primary antibody incubation. To label actin, we added phalloidin (P1951, Sigma) labeled
542 with Alexa-647 (0.094 µM in PBS) and incubated for 20 mins on 100 µL droplets in the
543 humid chamber. We transferred coverslips to PBS, then set up for imaging by sealing
544 them to a glass slide with double sided tape and vacuum grease to a glass slide and
545 adding PBS to the channel. Finally, we imaged the cells in ~1.5-2 µm thick z-stacks using
546 near-TIRF microscopy, with 1 mW laser power at 640 nm, 561 nm, and 488 nm excitation,
547 600 ms exposure time, EM gain of 200 using an EMCCD camera of a Nikon Eclipse Ti-E
548 microscope.
549
550 **Immunofluorescence: Motor Colocalization**
551 This protocol differs from cytoskeletal imaging in the fixation step; we incubated cells at -
552 20 °C with 1 mM EGTA (EGT101, Bioshop) in -20 °C methanol, for 8 mins. Subsequent
553 steps are identical to the cytoskeletal immunofluorescence protocol, except that the
554 blocking buffer contained 0.2% saponin (4521, Sigma). We first imaged cells for the motor
555 (kinesin or dynein) and saved their positions on the microscope. Following imaging, we
556 washed the sample and probed for tubulin while maintaining the slide in the same position
557 on the microscope, using another colour and shorter incubation times to allow higher
558 throughput. The protocol was as follows: 1 hr incubation with primary antibody, wash 3x

559 slide volume with blocking buffer, 45 mins incubation with secondary antibody, wash 3x
560 slide volume with PBS, this sequential antibody staining was done due to the redundancy
561 in antibody species available. The primary antibodies used for experiments were: 1/400
562 T9026 ms alpha-tubulin, Sigma lot: 000089497, 1/400 ms-kinesin heavy chain MAB1614
563 lot: 3593684, 1/400 MAB1618 ms-dynein, cytoplasmic lot: 3089121. Secondary
564 antibodies used for experiments were goat anti-mouse 488 (A21236, ThermoFisher) for
565 motors followed by Goat anti-mouse 647 (A21236, Sigma) for microtubules.
566
567 **Immunoflurescence: Huntingtin Localization**
568 We fixed the cells with prewarmed 4% paraformaldehyde at 37 °C for 10 mins, and
569 subsequently followed the protocol as outlined for cytoskeletal imaging. The huntingtin
570 antibody used was MAB2166 ms-huntingtin, Abcam lot: 3703568.The blocking buffer
571 contained 0.2% saponin (4521, Sigma).
572
573 **Immunofluorescence: Mitochondria**
574 We fixed cells using prewarmed 4% paraformaldehyde at 37 °C for 20 mins, followed by
575 3 washes with PBS. Using 50 mM NH_4Cl in PBS, we quenched fixation for 10 mins, and
576 washed again 3 times with PBS. We permeabilized cells using 0.1% TritonX-100 in PBS
577 for 10 mins with gentle rocking, followed by blocking with 10% BSA (ALB001, Bioshop)
578 for 30-45 mins with gentle rocking. We diluted the primary antibody 1/500 (TOMM40
579 18409-1-AP, Proteintech, Rosemont, IL, United States) with 5% BSA in PBS and
580 incubated overnight at 4 °C. We washed coverslips 3 times with gentle rocking using the
581 5% BSA in PBS. We diluted the secondary antibody 1/400 in the same solution and
582 incubated for 1 hr at room temperature. We repeated the washing described after the
583 primary antibody incubation, then mounted the slide using PBS as the imaging medium.
584 We imaged samples using an Olympus IX83 with a 100x objective using a disk scanning
585 unit to obtain high resolution z stacking in a 25 μm range using 0.5 μm slices.
586
587 **Intracellular Optical Tweezers**
588 We prepared a fibronectin (356008 Corning, Bedford, MA, United States) stock at a
589 concentration of 1.4 mg/mL in water and stored it at -20 °C until use. We coated

590 fluorescent yellow/green 500 nm beads (F8813, ThermoFisher Scientific) by centrifuging
591 20 μL of stock bead solution at 20000 rcf for 5 mins, then resuspended the beads in 25
592 μL of the fibronectin solution. We incubated the beads overnight at 4 °C, then washed
593 with 40 μL PBS 3 times, centrifuging again at 20000 rcf for 5 mins each. We diluted this
594 bead solution 1/20 in DMEM complete media, sonicated for 5 mins, and incubated with
595 the cells for 10 mins at 37 °C. For imaging, we replaced the medium with Lebovitz
596 supplemented with 10% FBS. Early endosome data was acquired from 15 mins–50 mins
597 after bead internalization, while lysosomes were from 1 - 2 hours post-internalization. We
598 identified cargoes moving processively within the cell, positioned the location of the center
599 of the optical tweezer laser above the motile cargo, and opened the shutter to capture the
600 bead. We acquired 60 s force traces holding the optical tweezer laser (12 W, 1064 nm)
601 fixed in the original capture position, while monitoring the position signal and live image
602 to ensure that the bead remained within one bead radius of the center of the tweezer.
603 Immediately after this measurement, we calibrated the optical tweezers by applying a 275
604 s multifrequency sinusoid to calculate the position sensitivity (β), trap stiffness (k_{trap}), and
605 viscoelastic properties (G', G'', Fig. S2E, F) of the cytoplasm as previously described
606 (Chaubet et al., 2020).
607
608 **Immunofluorescence Analysis: Actin, Microtubules, Golgi, Huntingtin**
609 For each z-stack, we chose the sharpest image for each channel for qualitative analysis
610 and observation as overlays.
611
612 **Mitochondrial Immunofluorescence Analysis**
613 We determined the range of z-values with samples in focus, and only used those slices
614 for image analysis. We processed the images in Fiji with the white top hat 3D
615 morphological filter, using a radius of 5 in x and y, and 2 in z. We then set an automatic
616 threshold and converted the thresholded image to a mask. Next, we ran the analyze
617 particles function to determine the shape, area, and number of mitochondria in each
618 plane, repeated for all in focus z planes, and added all the values for each z plane
619 together. We plotted the results from all cells using MATLAB.
620

621 **Golgi Dispersal Analysis**

622 Using ImageJ, we observed each of the Golgi images using the same linear LUT
623 (minimum = 145 a.u. and maximum = 1885 a.u.) and then categorized the Golgi into
624 organized, dispersed, or undetermined. Comparing the results from multiple experiments
625 using this binary categorization and excluding the undetermined data, we determined the
626 percentage of organized and dispersed Golgi observed in each cell type.

627

628 **Motility Assay Analysis- Tracking**

629 We used the Fiji plugin TrackMate (Tinevez et al., 2017) to generate tracks from the
630 images for subsequent analysis. The settings used in TrackMate highly influence the
631 results and are therefore shown in the tables below (Table 1 and 2). We chose the
632 parameters by comparing the maximum intensity projection of all frames with the
633 generated tracks and trying multiple values that would be considered logical for these
634 cargos.

635

636 **Table 1**. TrackMate analysis settings used in the analysis of lysosomal cargoes using LysoTracker™.

Parameter	Value
Estimated blob diameter	1 μm
Intensity threshold	400
Linking maximum distance	0.5 μm
Gap-closing maximum distance	0.5 μm
Gap-closing maximum frame gap	2

637

638 **Table 2.** TrackMate analysis settings used in the analysis of early endosomal cargoes using Rab5-eGFP
639 transfected cells.

Parameter	Value
Estimated blob diameter	0.8 μm
Intensity threshold	300
Linking maximum distance	0.5 μm
Gap-closing maximum distance	0.5 μm
Gap-closing maximum frame gap	2

640

641 **Motility Assay Analysis-Quantitation**

642 To analyze the raw TrackMate data, we wrote custom MATLAB codes, now available on
643 GitHub: https://github.com/hendricks-lab.
644
645 We calculated time averaged mean squared displacement according to the following
646 formula:

647 $$MSD = \frac{1}{\tau - t}\sum_{t=0}^{\tau-t}(x_{t+1} - x_t)^2$$

648
649 We calculated α values by fitting a line to the log-log plot of the mean squared
650 displacement for time delays from 120 ms-5 s. We obtained radius of gyration values
651 using the following formula:

652 $$R_g^2 = \frac{1}{N}\sum_{k=1}^{N}(r_k - r_{mean})^2$$

653
654 **Optical Tweezers: Force Trace Analysis**
655 We calculated the trap stiffness and position sensitivity from the calibration data as
656 previously described (Chaubet et al., 2020). Using the calibration data, we converted 60
657 s position traces to force traces (Fig. S2D) and calculated the viscoelastic moduli in each
658 condition (Fig. S2B, C). We observed brightfield images of the position of the trap and the
659 cell's nucleus to define the directionality of the cargo's movement. Any force event that
660 had a maximum off-axis force, a force in the direction perpendicular to the defined
661 microtubule axis, above 75% of the median on-axis forces, forces along the direction of
662 the microtubule, were excluded. Stall forces were binned into 1 pN size bins and counted
663 as stalls if the duration that they were above 0.5 pN duration was longer than 0.1 s. We
664 calculated binding rates from the force traces by identifying the times that the cargoes
665 unbound from the microtubules after a stall event and determining the time between
666 unbinding and rebinding to the microtubule. We calculated force-dependent unbinding
667 rates from the stall force event before a cargo became detached and categorized them
668 by the direction the cargo was travelling immediately prior to detachment, as previously
669 described (Berger et al., 2019). We performed an exponential fit to the data and presented

it in Table S1 following the equation below with U as the unbinding rate, U_0 as the force-independent unbinding rate, F as the force, and F_d as the detachment force.

$$U = U_0 e^{\frac{F}{F_d}}$$

Statistical Analysis

We analysed all pairwise histogram comparisons and cumulative distribution functions using the Kolmogorov-Smirnov (ks) test. We used Student's two-tailed t-test for all pairwise analyses of violin plots. For optical tweezers stall force distribution analyses, in addition to the ks test we performed bootstrapping. We took 1000 bootstrap means of samples equivalent to the number of datapoints for the condition being tested. We then calculated 95% confidence intervals from the bootstrap mean distribution using the quantile function in MATLAB. To calculate p-values for bootstrap samples (not reported in Fig. 3), we subtracted the control from the S421D condition for each of the 1000 bootstrap means for the conditions to be compared and plotted the distribution (Fig. S2E). The p-value was determined by the fraction of data that overlapped with the 0 value, if this fraction was lower than 0.05, the difference between the values was considered statistically significant.

ACKNOWLEDGEMENTS

We thank Frederic Saudou (U. Grenoble) for generously sharing huntingtin constructs, Amine Kamen (McGill U.) for guidance on CRISPR/Cas9, and the members of the Hendricks lab for thoughtful comments on the manuscript.

COMPETING INTERESTS

The authors report no competing interests.

FUNDING

ENPP is supported by a CGS-M fellowship from the Natural Sciences and Engineering Council of Canada. AGH is supported by the Canadian Institutes for Health Research (PJT-159490).

REFERENCES

701 **Al-Haddad, A., Shonn, M. A., Redlich, B., Blocker, A., Burkhardt, J. K., Yu, H.,**
702 **Hammer, J. A., Weiss, D. G., Steffen, W., Griffiths, G., et al.** (2001). Myosin Va
703 bound to phagosomes binds to F-actin and delays microtubule-dependent motility.
704 *Mol. Biol. Cell* **12**, 2742–2755.
705 **Bentley, M., Decker, H., Luisi, J. and Banker, G.** (2015). A novel assay reveals
706 preferential binding between rabs, kinesins, and specific endosomal
707 subpopulations. *J. Cell Biol.* **208**, 273–281.
708 **Berger, F., Klumpp, S. and Lipowsky, R.** (2019). Force-Dependent Unbinding Rate of
709 Molecular Motors from Stationary Optical Trap Data. *Nano Lett.* **19**, 2598–2602.
710 **Blehm, B. H., Schroer, T. A., Trybus, K. M., Chemla, Y. R. and Selvin, P. R.** (2013).
711 In vivo optical trapping indicates kinesin's stall force is reduced by dynein during
712 intracellular transport. *Proc. Natl. Acad. Sci. U. S. A.* **110**, 3381–3386.
713 **Blocker, A., Severin, F. F., Burkhardt, J. K., Bingham, J. B., Yu, H., Olivo, J. C.,**
714 **Schroer, T. A., Hyman, A. A. and Griffiths, G.** (1997). Molecular requirements for
715 bi-directional movement of phagosomes along microtubules. *J. Cell Biol.* **137**, 113–
716 129.
717 **Burkhardt, J. K., Echeverri, C. J., Nilsson, T. and Vallee, R. B.** (1997).
718 Overexpression of the dynamitin (p50) subunit of the dynactin complex disrupts
719 dynein-dependent maintenance of membrane organelle distribution. *J. Cell Biol.*
720 **Cason, S. E., Carman, P., Van Duyne, C., Goldsmith, J., Dominguez, R. and**
721 **Holzbaur, E. L. F.** (2021). Dynein effectors regulate autophagosome motility
722 Sequential dynein effectors regulate axonal autophagosome motility in a
723 maturation-dependent pathway. *J. Chem. Biol.*
724 **Caviston, J. P. and Holzbaur, E. L. F.** (2009). Huntingtin as an essential integrator of
725 intracellular vesicular trafficking. *Trends Cell Biol.*
726 **Caviston, J. P., Ross, J. L., Antony, S. M., Tokito, M. and Holzbaur, E. L. F.** (2007).
727 Huntingtin facilitates dynein/dynactin-mediated vesicle transport. *Proc. Natl. Acad.*
728 *Sci. U. S. A.* **104**, 10045–10050.
729 **Caviston, J. P., Zajac, A. L., Tokito, M. and Holzbaur, E. L. F.** (2011). Huntingtin
730 coordinates the dynein-mediated dynamic positioning of endosomes and
731 lysosomes. *Mol. Biol. Cell*.

732 **Chaubet, L., Chaudhary, A. R., Heris, H. K., Ehrlicher, A. J. and Hendricks, A. G.**
733 (2020). Dynamic actin cross-linking governs the cytoplasm's transition to fluid-like
734 behavior. *Mol. Biol. Cell* **31**, 1744–1752.
735 **Chaudhary, A. R., Berger, F., Berger, C. L. and Hendricks, A. G.** (2018). Tau directs
736 intracellular trafficking by regulating the forces exerted by kinesin and dynein
737 teams. *Traffic* **19**, 111–121.
738 **Chung, P. J., Song, C., Deek, J., Miller, H. P., Li, Y., Choi, M. C., Wilson, L.,**
739 **Feinstein, S. C. and Safinya, C. R.** (2016). Tau mediates microtubule bundle
740 architectures mimicking fascicles of microtubules found in the axon initial segment.
741 *Nat. Commun.* **7**, 1–9.
742 **Colin, E., Zala, D., Liot, G., Rangone, H., Borrell-Pagès, M., Li, X. J., Saudou, F.**
743 **and Humbert, S.** (2008). Huntingtin phosphorylation acts as a molecular switch for
744 anterograde/retrograde transport in neurons. *EMBO J.*
745 **Corthésy-Theulaz, I., Pauloin, A. and Pfeffer, S. R.** (1992). Cytoplasmic dynein
746 participates in the centrosomal localization of the Golgi complex. *J. Cell Biol.* **118**,
747 1333–1345.
748 **Dambournet, D., Sochacki, K. A., Cheng, A. T., Akamatsu, M., Taraska, J. W.,**
749 **Hockemeyer, D. and Drubin, D. G.** (2018). Genome-edited human stem cells
750 expressing fluorescently labeled endocytic markers allow quantitative analysis of
751 clathrin-mediated endocytosis during differentiation. *J. Cell Biol.* **217**, 3301–3311.
752 **Davies, S. W., Turmaine, M., Cozens, B. A., DiFiglia, M., Sharp, A. H., Ross, C. A.,**
753 **Scherzinger, E., Wanker, E. E., Mangiarini, L. and Bates, G. P.** (1997).
754 Formation of neuronal intranuclear inclusions underlies the neurological dysfunction
755 in mice transgenic for the HD mutation. *Cell*.
756 **Dunah, A. W., Jeong, H., Griffin, A., Kim, Y. M., Standaert, D. G., Hersch, S. M.,**
757 **Mouradian, M. M., Young, A. B., Tanese, N. and Krainc, D.** (2002). Sp1 and
758 TAFII130 transcriptional activity disrupted in early Huntington's disease. *Science*
759 *(80-.).* **296**, 2238–2243.
760 **Duyao, M. P., Auerbach, A. B., Ryan, A., Persichetti, F., Barnes, G. T., McNeil, S.**
761 **M., Ge, P., Vonsattel, J. P., Gusella, J. F., Joyner, A. L., et al.** (1995).
762 Inactivation of the mouse huntington's disease gene homolog Hdh. *Science (80-.).*

763 **269**, 407–410.
764 **Ebneth, A., Godemann, R., Stamer, K., Illenberger, S., Trinczek, B., Mandelkow, E.**
765 **M. and Mandelkow, E.** (1998). Overexpression of tau protein inhibits kinesin-
766 dependent trafficking of vesicles, mitochondria, and endoplasmic reticulum:
767 Implications for Alzheimer's disease. *J. Cell Biol.* **143**, 777–794.
768 **Encalada, S. E., Szpankowski, L., Xia, C. H. and Goldstein, L. S. B.** (2011). Stable
769 kinesin and dynein assemblies drive the axonal transport of mammalian prion
770 protein vesicles. *Cell* **144**, 551–565.
771 **Engelender, S.** (1997). Huntingtin-associated protein 1 (HAP1) interacts with the
772 p150Glued subunit of dynactin. *Hum. Mol. Genet.*
773 **Fu, M. M. and Holzbaur, E. L. F.** (2013). JIP1 regulates the directionality of APP axonal
774 transport by coordinating kinesin and dynein motors. *J. Cell Biol.*
775 **Fu, M. meng and Holzbaur, E. L. F.** (2014). Integrated regulation of motor-driven
776 organelle transport by scaffolding proteins. *Trends Cell Biol.*
777 **Futter, M., Diekmann, H., Schoenmakers, E., Sadiq, O., Chatterjee, K. and**
778 **Rubinsztein, D. C.** (2009). Wild-type but not mutant huntingtin modulates the
779 transcriptional activity of liver X receptors. *J. Med. Genet.* **46**, 438–446.
780 **Gauthier, L. R., Charrin, B. C., Borrell-Pagès, M., Dompierre, J. P., Rangone, H.,**
781 **Cordelières, F. P., De Mey, J., MacDonald, M. E., Leßmann, V., Humbert, S., et**
782 **al.** (2004). Huntingtin controls neurotrophic support and survival of neurons by
783 enhancing BDNF vesicular transport along microtubules. *Cell* **118**, 127–138.
784 **Gil, J. M. and Rego, A. C.** (2008). Mechanisms of neurodegeneration in Huntington's
785 disease. *Eur. J. Neurosci.*
786 **Goldman, A., Harper, S. and Speicher, D. W.** (2016). Detection of proteins on blot
787 membranes - Current Protocols in Protein Science. *Curr. Protoc. Protein Sci.* 1–6.
788 **Guo, Q., Huang, B., Cheng, J., Seefelder, M., Engler, T., Pfeifer, G., Oeckl, P., Otto,**
789 **M., Moser, F., Maurer, M., et al.** (2018). The cryo-electron microscopy structure of
790 huntingtin. **555**, 117–120.
791 **Hendricks, A. G., Perlson, E., Ross, J. L., Schroeder, H. W., Tokito, M. and**
792 **Holzbaur, E. L. F.** (2010). Motor Coordination via a Tug-of-War Mechanism Drives
793 Bidirectional Vesicle Transport. *Curr. Biol.*

794 **Hilditch-Maguire, P.** (2000). Huntingtin: an iron-regulated protein essential for normal
795 nuclear and perinuclear organelles. *Hum. Mol. Genet.*
796 **Holbert, S., Denghien, I., Kiechle, T., Rosenblatt, A., Wellington, C., Hayden, M. R.,**
797 **Margolis, R. L., Ross, C. A., Dausset, J., Ferrante, R. J., et al.** (2001). The Gln-
798 Ala repeat transcriptional activator CA150 interacts with huntingtin:
799 Neuropathologic and genetic evidence for a role in Huntington's disease
800 pathogenesis. *Proc. Natl. Acad. Sci. U. S. A.* **98**, 1811–1816.
801 **Humbert, S., Bryson, E. A., Cordelières, F. P., Connors, N. C., Datta, S. R.,**
802 **Finkbeiner, S., Greenberg, M. E. and Saudou, F.** (2002). The IGF-1/Akt pathway
803 is neuroprotective in Huntington's disease and involves huntingtin phosphorylation
804 by Akt. *Dev. Cell*.
805 **Jimenez, A., Friedl, K. and Leterrier, C.** (2020). About samples, giving examples:
806 Optimized Single Molecule Localization Microscopy. *Methods*.
807 **Leavitt, B. R., Van Raamsdonk, J. M., Shehadeh, J., Fernandes, H., Murphy, Z.,**
808 **Graham, R. K., Wellington, C. L., Raymond, L. A. and Hayden, M. R.** (2006).
809 Wild-type huntingtin protects neurons from excitotoxicity. *J. Neurochem.* **96**, 1121–
810 1129.
811 **Lemarié, F. L., Caron, N. S., Sanders, S. S., Schmidt, M. E., Nguyen, Y. T. N., Ko,**
812 **S., Xu, X., Pouladi, M. A., Martin, D. D. O. and Hayden, M. R.** (2021). Rescue of
813 aberrant huntingtin palmitoylation ameliorates mutant huntingtin-induced toxicity.
814 *Neurobiol. Dis.* **158**,.
815 **Li, S. H., Schilling, G., Young, W. S., Li, X., Margolis, R. L., Stine, O. C., Wagster,**
816 **M. V., Abbott, M. H., Franz, M. L., Ranen, N. G., et al.** (1993). Huntington's
817 disease gene (IT15) is widely expressed in human and rat tissues. *Neuron* **11**,
818 985–993.
819 **Li, S. H., Gutekunst, C. A., Hersch, S. M. and Li, X. J.** (1998). Interaction of
820 Huntingtin-associated protein with dynactin P150(Glued). *J. Neurosci.*
821 **Li, S.-H., Cheng, A. L., Zhou, H., Lam, S., Rao, M., Li, H. and Li, X.-J.** (2002).
822 Interaction of Huntington Disease Protein with Transcriptional Activator Sp1. *Mol.*
823 *Cell. Biol.* **22**, 1277–1287.
824 **Liot, G., Zala, D., Pla, P., Mottet, G., Piel, M. and Saudou, F.** (2013). Mutant

825 huntingtin alters retrograde transport of TrkB receptors in striatal dendrites. *J.*
826 *Neurosci.* **33**, 6298–6309.
827 **Lo Sardo, V., Zuccato, C., Gaudenzi, G., Vitali, B., Ramos, C., Tartari, M., Myre, M.**
828 **A., Walker, J. A., Pistocchi, A., Conti, L., et al.** (2012). An evolutionary recent
829 neuroepithelial cell adhesion function of huntingtin implicates ADAM10-Ncadherin.
830 *Nat. Neurosci.* **15**, 713–721.
831 **Marcora, E., Gowan, K. and Lee, J. E.** (2003). Stimulation of NeuroD activity by
832 huntingtin and huntingtin-associated proteins HAP1 and MLK2. *Proc. Natl. Acad.*
833 *Sci. U. S. A.* **100**, 9578–9583.
834 **McGuire, J. R., Rong, J., Li, S. H. and Li, X. J.** (2006). Interaction of Huntingtin-
835 associated protein-1 with kinesin light chain: Implications in intracellular trafficking
836 in neurons. *J. Biol. Chem.* **281**, 3552–3559.
837 **McKenney, R. J., Huynh, W., Tanenbaum, M. E., Bhabha, G. and Vale, R. D.** (2014).
838 Activation of cytoplasmic dynein motility by dynactin-cargo adapter complexes.
839 *Science (80-.).*
840 **Mogre, S. S., Christensen, J. R., Reck-Peterson, S. L. and Koslover, E. F.** (2021).
841 Optimizing microtubule arrangements for rapid cargo capture. *Biophys. J.* **120**,
842 4918–4931.
843 **Nasir, J., Floresco, S. B., O'Kusky, J. R., Diewert, V. M., Richman, J. M., Zeisler, J.,**
844 **Borowski, A., Marth, J. D., Phillips, A. G. and Hayden, M. R.** (1995). Targeted
845 disruption of the Huntington's disease gene results in embryonic lethality and
846 behavioral and morphological changes in heterozygotes. *Cell* **81**, 811–823.
847 **Pardo, R., Molina-Calavita, M., Poizat, G., Keryer, G., Humbert, S. and Saudou, F.**
848 (2010). PARIS-htt: An optimised expression platform to study huntingtin reveals
849 functional domains required for vesicular trafficking. *Mol. Brain* **3**, 1–17.
850 **Reed, N. A., Cai, D., Blasius, T. L., Jih, G. T., Meyhofer, E., Gaertig, J. and Verhey,**
851 **K. J.** (2006). Microtubule Acetylation Promotes Kinesin-1 Binding and Transport.
852 *Curr. Biol.*
853 **Sahlender, D. A., Roberts, R. C., Arden, S. D., Spudich, G., Taylor, M. J., Luzio, J.**
854 **P., Kendrick-Jones, J. and Buss, F.** (2005). Optineurin links myosin VI to the
855 Golgi complex and is involved in Golgi organization and exocytosis. *J. Cell Biol.*

856 **Sanjana, N. E., Shalem, O. and Zhang, F.** (2014). Improved vectors and genome-wide
857 libraries for CRISPR screening HHS Public Access Supplementary Material. *Nat*
858 *Methods* **11**, 783–784.
859 **Saudou, F. and Humbert, S.** (2016). The Biology of Huntingtin. *Neuron*.
860 **Schlager, M. A., Hoang, H. T., Urnavicius, L., Bullock, S. L. and Carter, A. P.**
861 (2014). In vitro reconstitution of a highly processive recombinant human dynein
862 complex . *EMBO J.* **33**, 1855–1868.
863 **Schmitt, I., Bächner, D., Megow, D., Henkiein, P., Hamelster, H., Epplen, J. T. and**
864 **Riess, O.** (1995). Expression of the huntington disease gene in rodents: Cloning
865 the rat homologue and evidence for downregulation in non-neuronal tissues during
866 development. *Hum. Mol. Genet.* **4**, 1173–1182.
867 **Sharp, A. H., Loev, S. J., Schilling, G., Li, S. H., Li, X. J., Bao, J., Wagster, M. V.,**
868 **Kotzuk, J. A., Steiner, J. P., Lo, A., et al.** (1995). Widespread expression of
869 Huntington's disease gene (IT15) protein product. *Neuron* **14**, 1065–1074.
870 **Steffan, J. S., Agrawal, N., Pallos, J., Rockabrand, E., Trotman, L. C., Slepko, N.,**
871 **Illes, K., Lukacsovich, T., Zhu, Y. Z., Cattaneo, E., et al.** (2004). SUMO
872 Modification of Huntingtin and Huntington's Disease Pathology. *Science (80-.).*
873 **304**, 100–104.
874 **Sun, T., Li, Y., Li, T., Ma, H., Guo, Y., Jiang, X., Hou, M., Huang, S. and Chen, Z.**
875 (2017). JIP1 and JIP3 cooperate to mediate TrkB anterograde axonal transport by
876 activating kinesin-1. *Cell. Mol. Life Sci.*
877 **Thion, M. S., McGuire, J. R., Sousa, C. M., Fuhrmann, L., Fitamant, J., Leboucher,**
878 **S., Vacher, S., Du Montcel, S. T., Bièche, I., Bernet, A., et al.** (2015). Unraveling
879 the Role of Huntingtin in Breast Cancer Metastasis. *J. Natl. Cancer Inst.* **107**, 1–13.
880 **Tinevez, J. Y., Perry, N., Schindelin, J., Hoopes, G. M., Reynolds, G. D., Laplantine,**
881 **E., Bednarek, S. Y., Shorte, S. L. and Eliceiri, K. W.** (2017). TrackMate: An open
882 and extensible platform for single-particle tracking. *Methods* **115**, 80–90.
883 **Twelvetrees, A. E., Yuen, E. Y., Arancibia-Carcamo, I. L., MacAskill, A. F.,**
884 **Rostaing, P., Lumb, M. J., Humbert, S., Triller, A., Saudou, F., Yan, Z., et al.**
885 (2010). Delivery of GABAARs to Synapses Is Mediated by HAP1-KIF5 and
886 Disrupted by Mutant Huntingtin. *Neuron* **65**, 53–65.

887 **Wanker, E. E., Ast, A., Schindler, F., Trepte, P. and Schnoegl, S.** (2019). The
888 pathobiology of perturbed mutant huntingtin protein–protein interactions in
889 Huntington's disease. *J. Neurochem.* **151**, 507–519.
890 **Wong, Y. C. and Holzbaur, E. L. F.** (2014). The regulation of autophagosome
891 dynamics by huntingtin and HAP1 is disrupted by expression of mutant huntingtin,
892 leading to defective cargo degradation. *J. Neurosci.*
893 **Xu, X., Ng, B., Sim, B., Radulescu, C. I., Yusof, N. A. B. M., Goh, W. I., Lin, S., Lim,**
894 **J. S. Y., Cha, Y., Kusko, R., et al.** (2020). pS421 huntingtin modulates
895 mitochondrial phenotypes and confers neuroprotection in an HD hiPSC model. *Cell*
896 *Death Dis.*
897 **Yanai, A., Huang, K., Kang, R., Singaraja, R. R., Arstikaitis, P., Gan, L., Orban, P.**
898 **C., Mullard, A., Cowan, C. M., Raymond, L. A., et al.** (2006). Palmitoylation of
899 huntingtin by HIP14is essential for its trafficking and function. *Nat. Neurosci.* **9**,
900 824–831.
901 **Zala, D., Colin, E., Rangone, H., Liot, G., Humbert, S. and Saudou, F.** (2008).
902 Phosphorylation of mutant huntingtin at S421 restores anterograde and retrograde
903 transport in neurons. *Hum. Mol. Genet.*
904 **Zeitlin, S., Liu, J., Chapman, D. L. and Papaioannou, V. E.** (1995). article nullizygous
905 for the Huntington ' s disease gene homo logue. **11**, 155–163.
906 **Zuccato, C., Tartari, M., Crotti, A., Goffredo, D., Valenza, M., Conti, L., Cataudella,**
907 **T., Leavitt, B. R., Hayden, M. R., Timmusk, T., et al.** (2003). Huntingtin interacts
908 with REST/NRSF to modulate the transcription of NRSE-controlled neuronal genes.
909 *Nat. Genet.* **35**, 76–83.
910
911

912 **FIGURE LEGENDS**

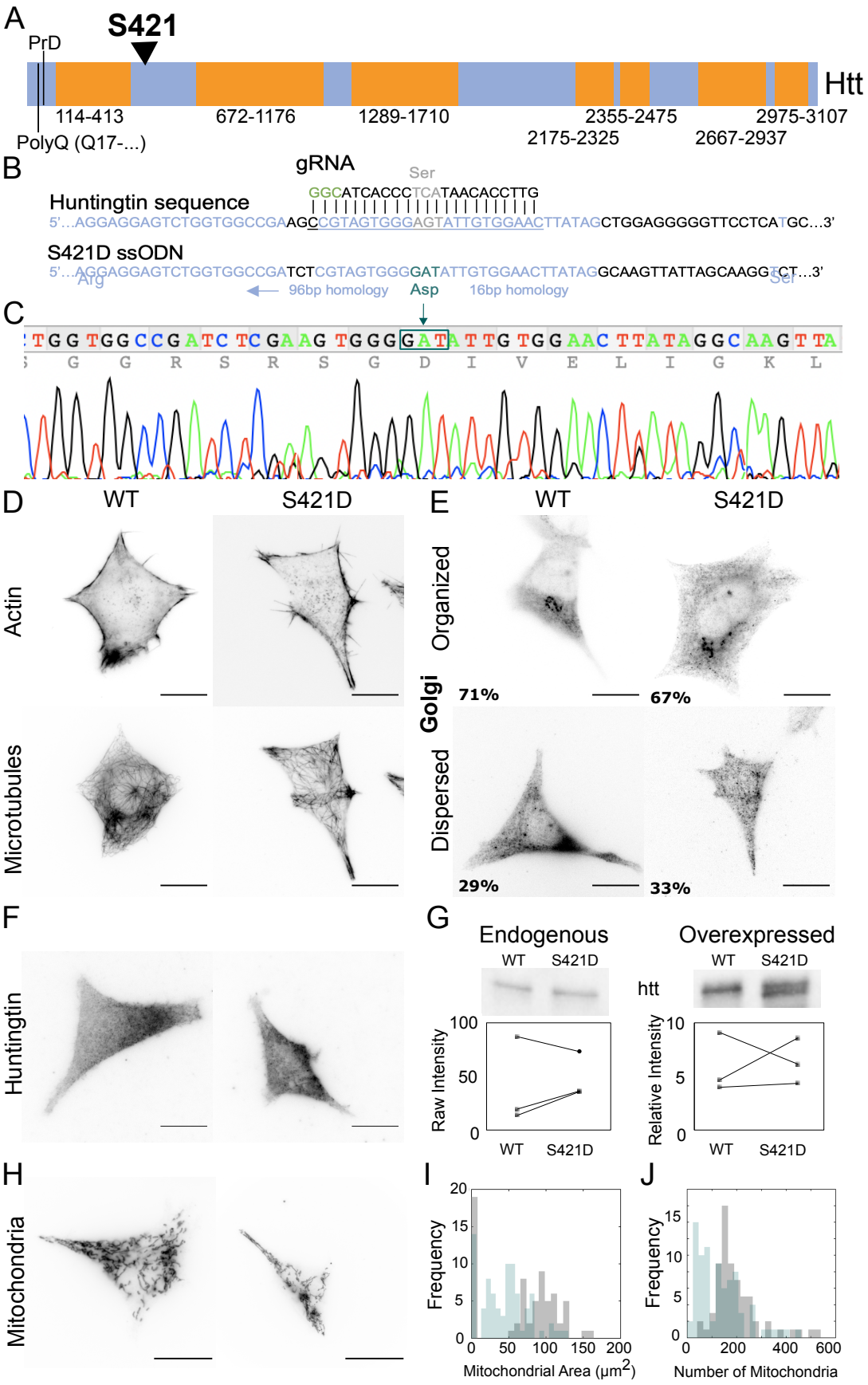
A
S421
PrD
Htt
114-413
672-1176
1289-1710
2355-2475
2975-3107
2175-2325
2667-2937
PolyQ (Q17-...)
B
gRNA
Ser
GGCATCACCCTCATAACACCTTG
Huntingtin sequence
5'...AGGAGGAGTCTGGTGGCCGAAGCCGTAGTGGGAGTATTGTGGAACTTATAGCTGGAGGGGGTTCCTCATGC...3'
S421D ssODN
5'...AGGAGGAGTCTGGTGGCCGATCTCGTAGTGGGGATATTGTGGAACTTATAGGCAAGGTCT...3'
Arg
96bp homology
Asp
16bp homology
Ser
C
D
WT
S421D
Actin
Microtubules
E
WT
S421D
Organized
Golgi
Dispersed
71%
67%
29%
33%
F
Huntingtin
G
Endogenous
Overexpressed
WT
S421D
htt
Raw Intensity
Relative Intensity
H
Mitochondria
I
Frequency
Mitochondrial Area (μm2)
J
Frequency
Number of Mitochondria

913

Fig. 1. S421D HEK293T cell line does not affect cytoskeletal organization, huntingtin localization, or dynein function. (A) Huntingtin protein sequence schematic demonstrating the structured domains (HEAT repeats and other α-helical regions, orange), unstructured domains (blue), S421 phosphosite, polyglutamine repeat region (PolyQ), and proline rich domain (PrD). (B) CRISPR phosphomimetic mutant design guide RNA (gRNA), and ssODN homologous recombination template. (C) Chromatogram of the positive clone containing the phosphomimetic mutation S421D. (D) Immunostaining of actin (top) and microtubules (bottom) indicating no difference between WT (left) and S421D (right) HEK293T cells. Note immunofluorescence images are inverted such that the protein of interest is dark, and the background is white, and all scale bars in the figure are 20 μm. (E) In both WT and S421D HEK293T cells, the Golgi apparatus appeared compact (organized) in ~70% of cells and dispersed in ~30% of cells. WT data for actin, microtubules, and Golgi apparatus staining was from 14 experiments, 84 cells, and S421D data from 11 experiments, 69 cells. (F) Immunofluorescence of huntingtin protein localization in WT (left) compared to S421D (right) HEK293T cells. Immunofluorescence of huntingtin localization for WT cells from 3 experiments, 43 cells and for S421D from 2 experiments, 22 cells. (G) WT and S421D huntingtin endogenous expression levels (top left) detected by Western blot with the raw intensity data from three independent samples (bottom left), compared to levels when overexpressing full length mCherry-WT or mCherry S421D huntingtin (top right) and the fold change relative to native expression levels for three independent samples (bottom right). Samples collected on the same date are connected by a line. (H) Mitochondrial morphology of WT (left) and S421D (right) HEK293T cells. (I) Mitochondrial area of WT (grey) compared to S421D (blue) cells, $p=6.59\times10^{-8}$ by Kolmogorov-Smirnov (ks) test. (J) Number of mitochondria per cell in WT (grey) compared to S421D (blue), $p=6.14\times10^{-7}$ by ks test. Mitochondrial analysis for WT from 7 experiments, 88 cells, and S421D from 7 experiments, 94 cells.

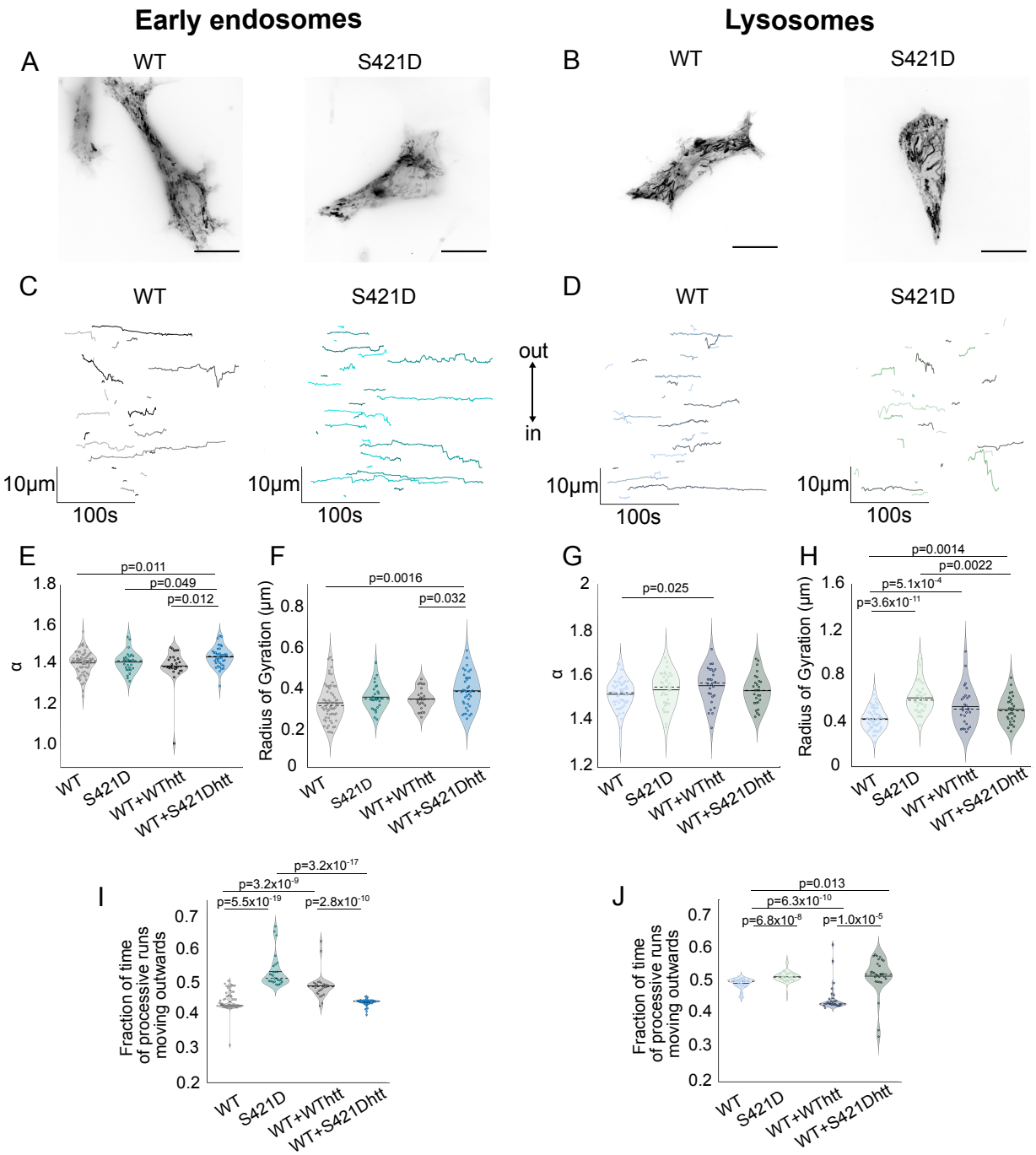

Fig. 2. Huntingtin S421D mutation increases outward motility of early endosomes and lysosomes while overexpression affects all parameters. (A, B) Maximum intensity projection of early endosomes, labelled with Rab5-eGFP, and lysosomes, labelled with Lysotracker, for endogenous WT and S421D huntingtin expressing cells. All scale bars are 20 µm. (C, D) Sample trajectories for early endosomes (C) and lysosomes (D) in both WT and S421D huntingtin endogenously expressing cells, with their inward (in) or outward (out) directionality indicated by the arrows in the center. Different shades of colours were assigned randomly to facilitate visualization of overlapping segments. (E, G) Early endosome (E) and lysosome (G) processivity per cell, measured by α, the slope of the log-log plot of their mean-squared displacement. Means are represented with a filled line, while medians are dashed lines. (F. H) Radius of gyration (R_g) per cell of early endosomes (F) and lysosomes (H). R_g is a measure of the radius that contains half of the datapoints in the trajectory centered around its average position. (I, J) Early endosome (I) and

948 lysosome (J) directional bias per cell of processive trajectories toward plus ends of microtubules (outwards),
949 the remaining fraction of processive trajectories move inwards. Overexpression conditions represented by
950 +WThtt or +S421Dhtt. Directional bias is determined by fraction of time particles are moving outwards
951 compared to inwards and averaged for each cell. The number of experiments, cells, and trajectories for
952 each condition are the following; WT early endosomes: 65 cells, 41994 trajectories, 6 experiments; S421D
953 early endosomes: 28 cells, 25476 trajectories, 3 experiments; WT+WThtt early endosomes: 28 cells, 17424
954 trajectories, 5 experiments, WT+S421Dhtt early endosomes: 39 cells, 22854 trajectories, 6 experiments;
955 WT lysosomes: 55 cells, 25247 trajectories, 5 experiments; S421D lysosomes: 38 cells, 12670 trajectories,
956 4 experiments; WT+WThtt lysosomes: 29 cells, 7558 trajectories, 5 experiments; WT+S421Dhtt lysosomes:
957 28 cells, 7031 trajectories, 6 experiments. Statistical significance was determined via Student's two-tailed
958 t-test and p-values are indicated on each plot where applicable.
959

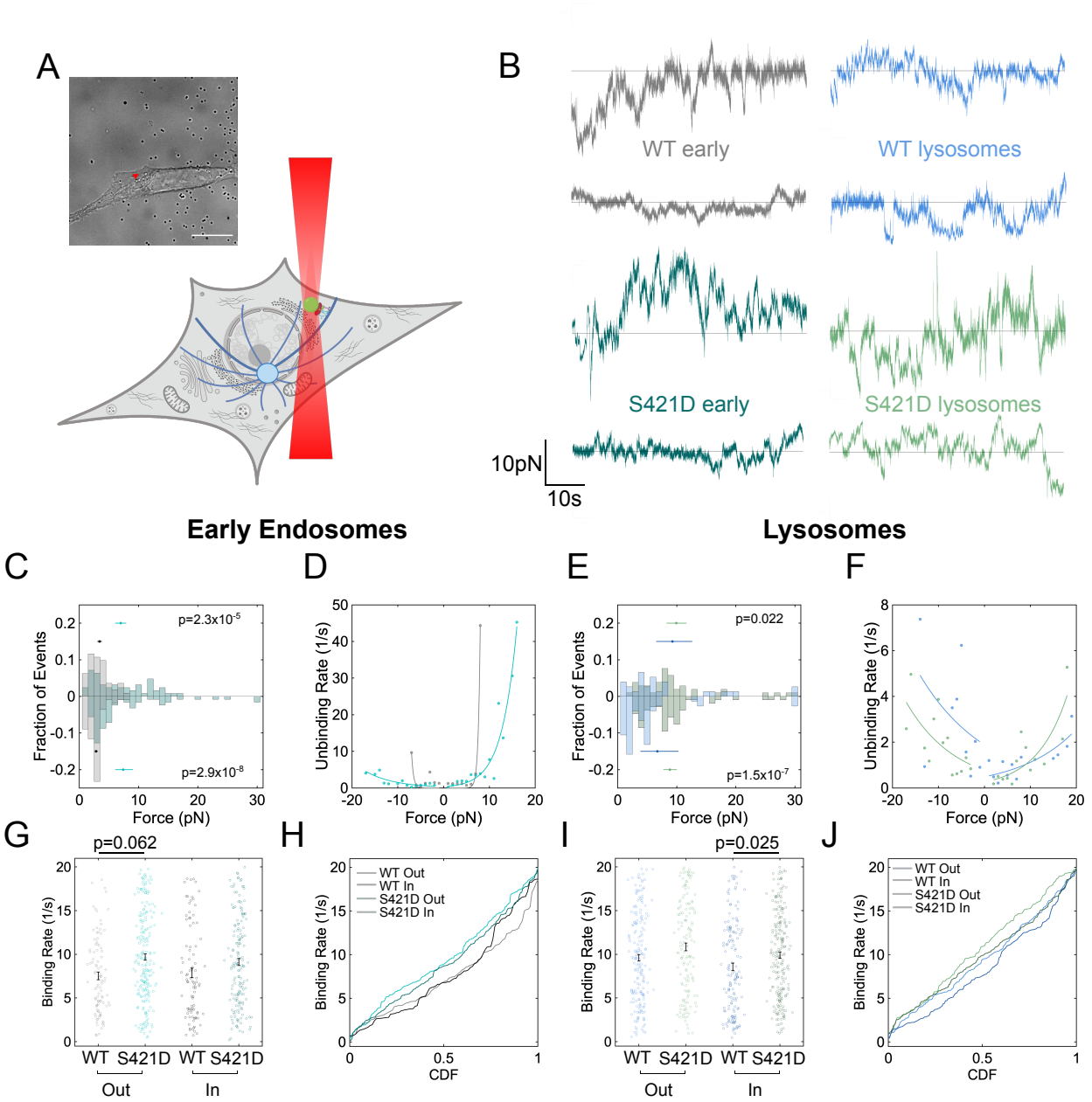

Fig. 3. Force trace analysis demonstrates S421D huntingtin induces higher binding rates, stronger binding, and higher forces in both directions for early endosomes and lysosomes. (A) Schematic of the optical tweezers assay including the endocytosed bead (green) inside the optical trap (red) along with a brightfield image of a cell during the experiment (top right). The scale bar is 20 μm and the arrowhead indicates the position of the optical trap during the experiment. (B) Sample force traces for early endosomes (early) and lysosomes in WT and S421Dhtt cells. The horizontal line indicates the zero axis, while positive values indicate outward forces and negative values indicate inward forces. (C, E) The fraction of early endosome or lysosome stall events at a given force with a minimum stall duration of 0.1 s, separated into 1 pN bins with the mean and 95% confidence intervals of bootstrap sampled means and p-values for each condition are shown above (for outward) or below (for inward) the distribution. The colours in (C-J) follow the colour legend from (B). (D, F) Force-dependent unbinding rates in both outward and inward directions (filled circles) for early endosomes or lysosomes fit with a single exponential (solid line). (G-J) Binding rates

for each stall event in early endosomes and lysosomes of WT and S421D in both directions in (G, I) including the cumulative distribution function (CDF) for each condition in (H, J). Statistical significance by ks test is indicated by the p-value in the figure panel where applicable. All results from optical tweezers data for WT early endosomes from 10 cells, 5 experiments; S421D early endosomes: 16 cells, 8 experiments; WT lysosomes: 12 cells, 5 experiments, S421D lysosomes: 11 cells, 4 experiments. Statistical significance was determined by ks test for binding rates and force distributions and p-values are indicated where applicable.

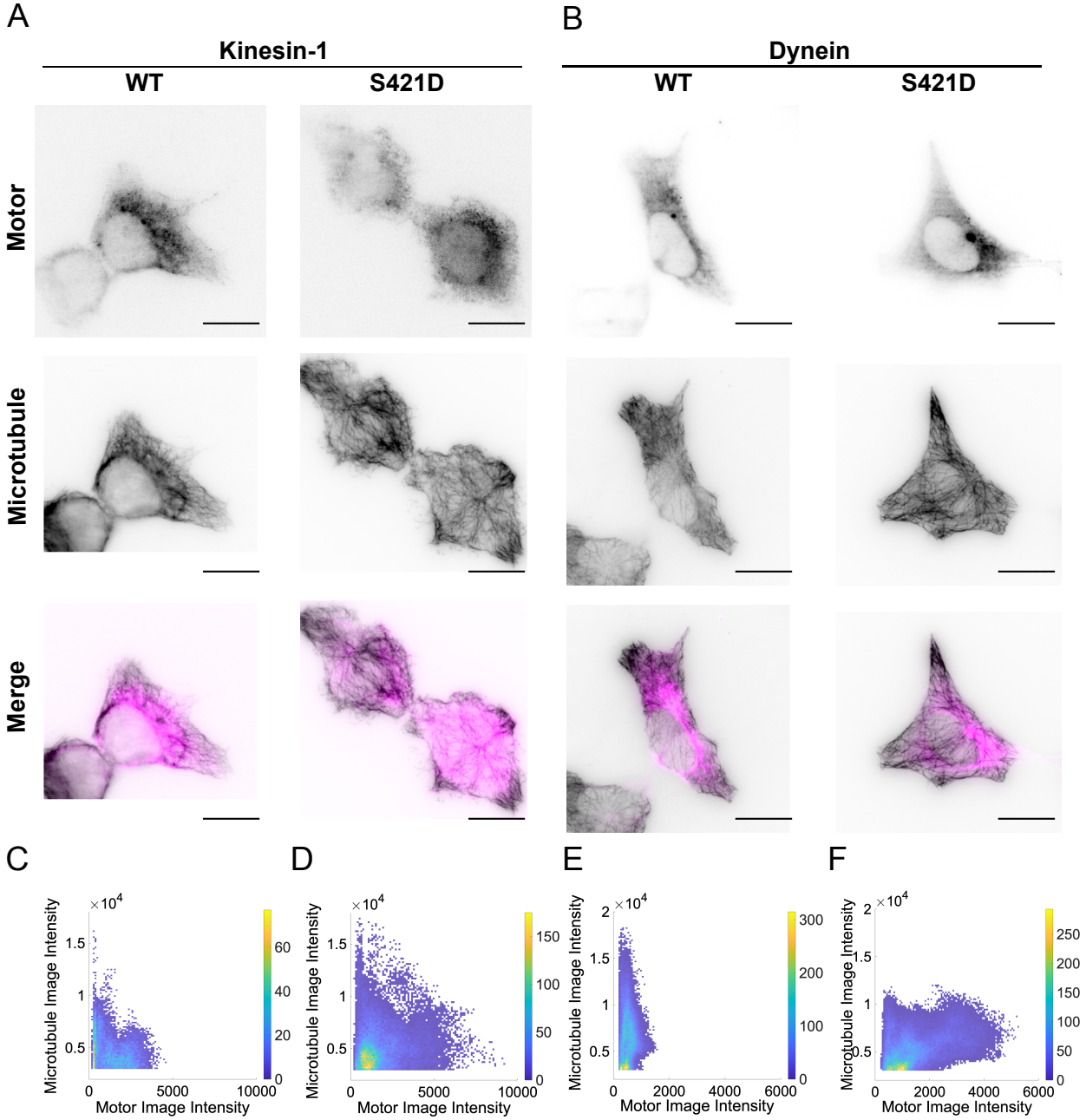

Fig. 4. S421D huntingtin increases kinesin and dynein association to extracted microtubules. (A, B) Inverted immunofluorescence images demonstrating colocalization (bottom) kinesin heavy chain (kinesin-1, (A), top) or dynein intermediate chain (dynein, (B), top) on extracted microtubules (middle) in WT and S421D huntingtin cells. In the merge channel, motors (kinesin-1 or dynein) are indicated in magenta and microtubules in black. All scale bars are 20 μm. (C-F) Colocalization plots were created from plotting intensity values of each pixel of the microtubule and motor (kinesin or dynein) channels of all images.

Differences between kinesin-1 WT and S421D correlation coefficients resulted in p=0.4748, while dynein WT compared to S421D correlation gave p=0.0533 by a two-tailed Student's t-test. Data for WT kinesin-1 from 17 cells, 3 experiments, S421D kinesin-1: 15 cells, 2 experiment, WT dynein: 32 cells, 4 experiments, and S421D dynein: 32 cells, 4 experiments.

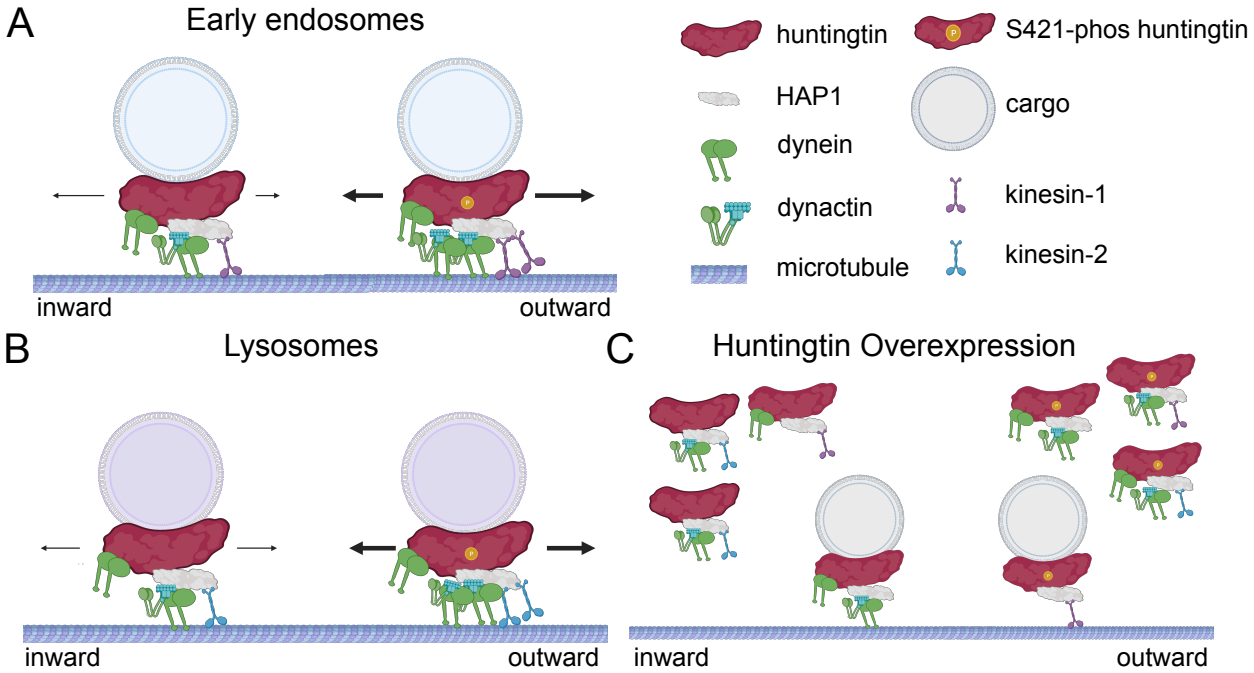

Fig. 5. Model of huntingtin S421 phosphorylation and expression level mediating regulation of early endosome and lysosome transport. (A) Huntingtin S421 phosphorylation (S421-phos) increases activity of kinesin and dynein motor proteins on early endosomes, such that the predominantly inward motility shifts to being more outward. (B) Lysosomes move bidirectionally. When kinesin and dynein activity are enhanced by huntingtin phosphorylation, the movement remains bidirectional, but the displacement of trajectories increases. (C) Overexpression sequesters motors and adaptors or disrupts vesicle-bound huntingtin-adaptor-motor complexes regardless of cargo identity or huntingtin phosphorylation state.

1003 **SUPPLEMENTARY MATERIALS**

1004

1005 **Table S1. Calculated parameters from exponential fits for unbinding rates of early endosomes and**
1006 **lysosomes.**

Condition	U_0	F_d (pN)
Early endosome WT outward	2.1×10^{-7}	0.42
Early endosome S421D outward	0.31	3.2
Early endosome WT inward	7.2×10^{-7}	0.43
Early endosome S421D inward	0.31	6.3
Lysosome WT outward	0.49	12.1
Lysosome S421D outward	0.24	6.6
Lysosome WT inward	1.9	14.6
Lysosome S421D inward	0.77	10.8

1007

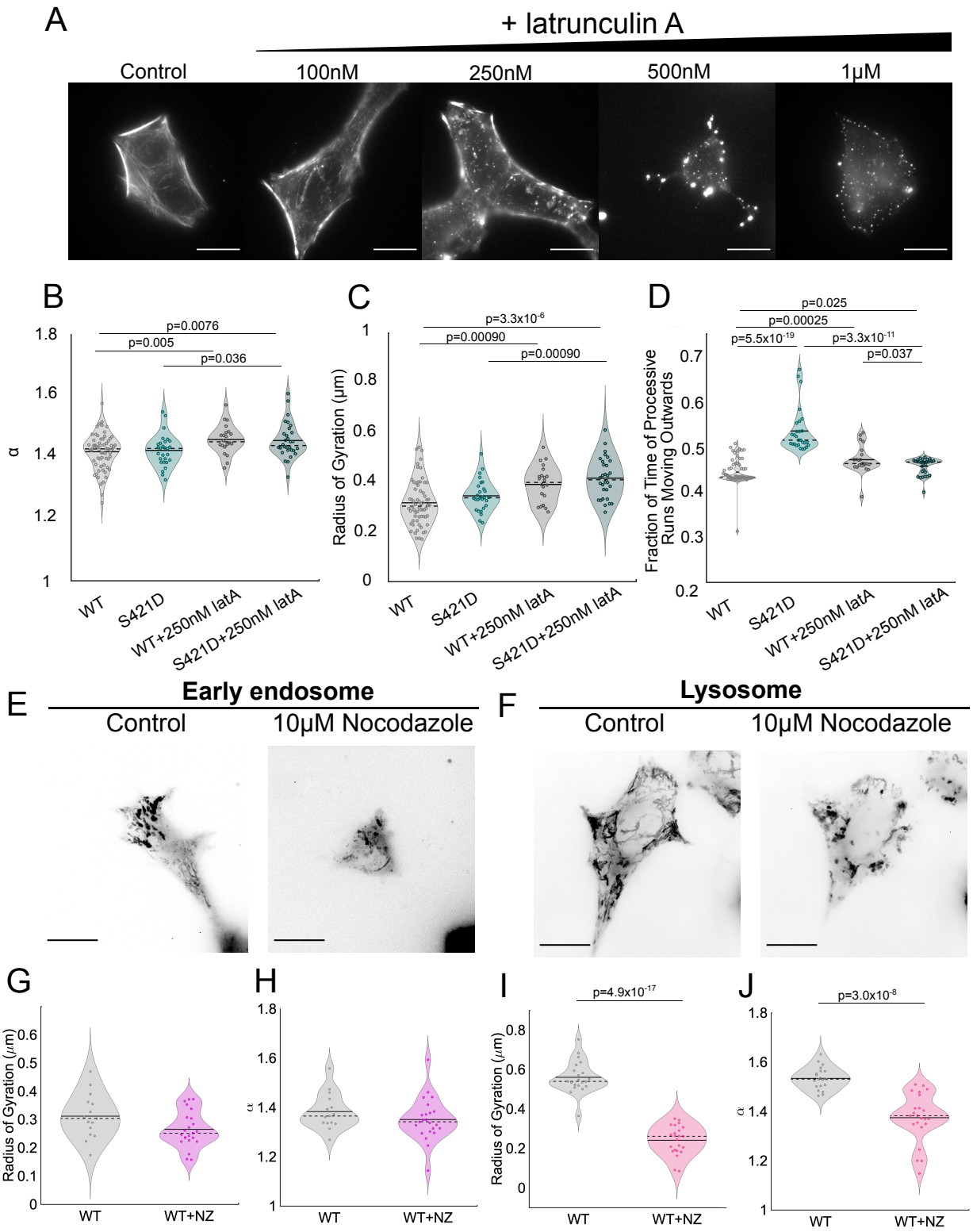

Fig. S1. Cytoskeletal disruption affects cargo motility. (A) Actin cytoskeleton labelled with SiR actin in S421D HEK293T cells treated with 100 nM-1 μM concentrations of latrunculin A (latA). Scale bars for all images are 20 μm, all images inverted. (B) Per cell α values of Rab5-eGFP labelled early endosomes. Means are represented with a filled line, while medians are dashed lines. (C) Radius of gyration (R_g) per cell is presented for early endosomes (C). (D) Directional bias per cell shown by fraction of time processive

1014 runs moving outward for Rab5-eGFP early endosomes. Note: control WT and S421D data for latrunculin A
1015 experiments is the same data reported in Fig. 2. (E, F) Maximum projections of the same cell with and
1016 without nocodazole (NZ) for early endosome and lysosome analysis. (G-J), Radius of gyration and alpha
1017 values for early endosomes and lysosomes before and after nocodazole treatment. (B-D) WT control data
1018 from 7 independent experiments (41994 trajectories, 64 cells), S421D data from 3 independent experiments
1019 (25476 trajectories, 28 cells), WT latA data from 3 independent experiments (17461 trajectories, 22 cells);
1020 S421D latA data from 5 independent experiments (19879 trajectories, 30 cells). (G, H) WT control data
1021 from 4 experiments, 22 cells, 6109 trajectories and WT+nocodazole data is from 4 experiments, 23 cells,
1022 and 7094 trajectories. (I, J) Contains control data from 4 experiments, 15 cells, 17073 trajectories, and
1023 nocodazole treated data from 4 experiments, 23 cells, and 6639 trajectories. Statistical significance of
1024 $p<0.05$ by Student's two sample t-test indicated in the figure where applicable.
1025

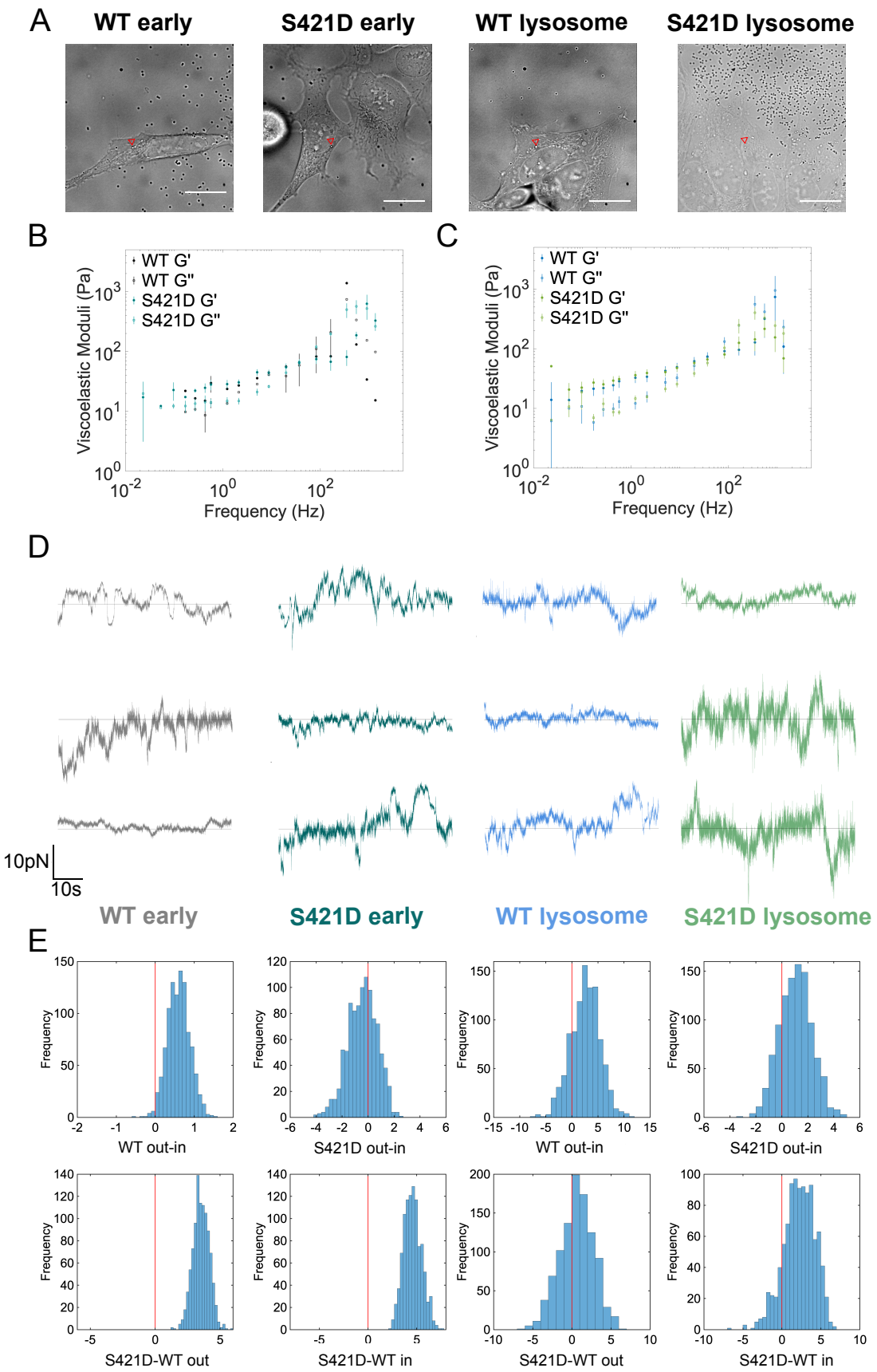
A
WT early
S421D early
WT lysosome
S421D lysosome
B
WT G'
WT G"
S421D G'
S421D G"
Viscoelastic Moduli (Pa)
Frequency (Hz)
C
WT G'
WT G"
S421D G'
S421D G"
Viscoelastic Moduli (Pa)
Frequency (Hz)
D
10pN
10s
WT early
S421D early
WT lysosome
S421D lysosome
E
Frequency
WT out-in
S421D out-in
WT out-in
S421D out-in
S421D-WT out
S421D-WT in
S421D-WT out
S421D-WT in

1026

Fig. S2. Force measurement analysis approach, additional force traces, and viscoelastic properties of WT and S421D huntingtin cells. (A) Brightfield image of a WT and S421D cell containing a trapped phagocytosed 500 nm bead (red arrow) during measurement of early endosome (early) or lysosome forces. (B, C) Viscous (G'') and elastic moduli (G') for WT (black) and S421D (teal) early endosomes and WT (blue) and S421D (green) lysosomes. (D) Additional sample force traces for each condition in optical tweezers assays, the horizontal line indicates the zero axis. Positive value forces are directed outward and negative forces are directed inward. (E) Distributions of bootstrap mean differences evaluated for additional statistical analysis of force distributions for the differences shown on the x axis of each plot in both early (left) and late (right) endosomes.

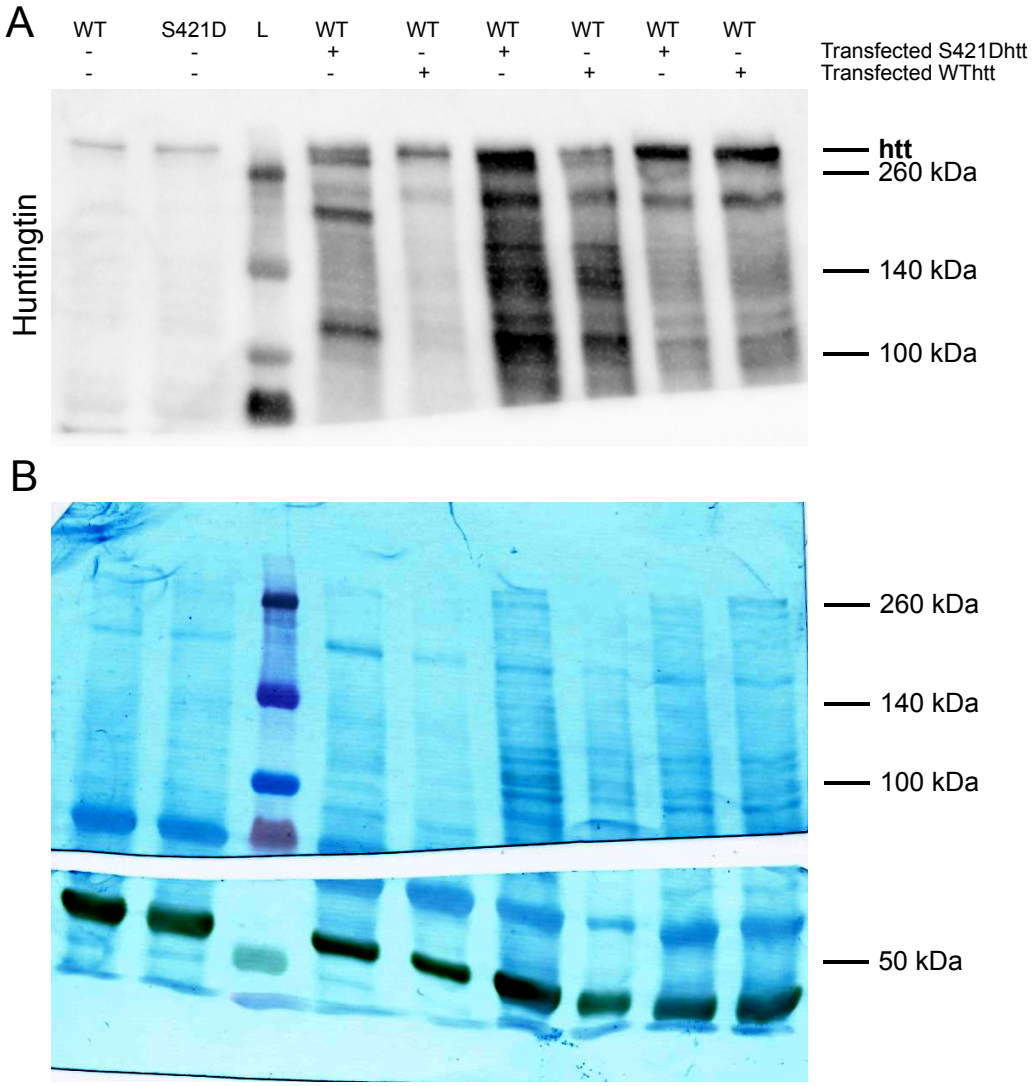

Fig. S3. Western blot transparency for huntingtin blot in Fig. 1. (A) Full western blot (above 100 kDa) of the blot presented in Fig. 1G using the anti-huntingtin antibody. Ladder is indicated by L with molecular weights to the right of the blot. (B) Coomassie staining of the entire membrane post-antibody staining.